ELSEVIER

Physica D 138 (2000) 1–43

PHYSICA D

www.elsevier.com/locate/physd

The Lorenz–Fermi–Pasta–Ulam experiment

N.J. Balmforth, C. Pasquero, A. Provenzale *

Consiglio Nazionale delle Ricerche, Istituto di Cosmogeofisica, Corso Fiume 4, I-10133 Torino, Italy

Received 4 February 1999; received in revised form 23 August 1999; accepted 2 September 1999
Communicated by C.K.R.T. Jones

Abstract

We consider a chain of Lorenz '63 systems connected through a local, nearest-neighbour coupling. We refer to the resulting system as the *Lorenz–Fermi–Pasta–Ulam* lattice because of its similarity to the celebrated experiment conducted by Fermi, Pasta and Ulam. At large coupling strengths, the systems synchronize to a global, chaotic orbit of the Lorenz attractor. For smaller coupling, the synchronized state loses stability. Instead, steady, spatially structured equilibrium states are observed. These steady states are related to the heteroclinic orbits of the system describing stationary solutions to the partial differential equation that emerges on taking the continuum limit of the lattice. Notably, these orbits connect saddle-foci, suggesting the existence of a multitude of such equilibria in relatively wide systems. On lowering the coupling strength yet further, the steady states lose stability in what appear to be always subcritical Hopf bifurcations. This can lead to a variety of time-dependent states with fixed time-averaged spatial structure. Such solutions can be limit cycles, tori or possibly chaotic attractors. "Cluster states" can also occur (though with less regularity), consisting of lattices in which the elements are partitioned into families of synchronized subsystems. Ultimately, for very weak coupling, the lattice loses its time-averaged spatial structure. At this stage, the properties of the lattice are probably chaotic and approximately scale with the lattice size, suggesting that the system is essentially an ensemble of elements that evolve largely independent of one another. The weak interaction, however, is sufficient to induce widespread *coherent phases*; these are ephemeral states in which the dynamics of one or more subsystems takes a more regular form. We present measures of the complexity of these *incoherent* lattices, and discuss the concept of a "dynamical horizon" (that is, the distance along the lattice that one subsystem can effectively influence another) and error propagation (how the introduction of a disturbance in one subsystem becomes spread throughout the lattice).

PACS: 47.52.+j; 05.45.+b

Keywords: Coupled dynamical systems; Synchronization; Coherent behaviour; Lorenz system

1. Introduction

In 1955, in what is now a classical paper in mathematical physics, Fermi et al. [1] described a computer experiment that was intended to observe the relaxation of a chain of coupled oscillators to equipartition in energy. However, what was observed in the actual experiment was anything but equipartition, with the energy in phase space sloshing back and forth in an apparently coherent, and strongly nonlinear, fashion; the energy localized repeatedly in only a few oscillators.

* Corresponding author. Fax: +39-11-6604056.
E-mail address: anto@icg.to.infn.it (A. Provenzale).

0167-2789/00/$ – see front matter
PII: S0167-2789(99)00193-1

Somewhat later, this recurrence was rationalized by Zabusky and Kruskal [2] on the basis of the continuum limit of the oscillator chain which turned out to be the celebrated Korteweg–de Vries equation. That observation was the beginning of the theory of solitons, one of the major developments in mathematical physics in this part of the last century.

In this article, we return to the Fermi–Pasta–Ulam experiment, but explore a slightly different version of the problem. Instead of coupling oscillators, we take a set of low-dimensional chaotic systems and explore the consequences of chaining them together. More specifically, we couple together a large number of Lorenz '63 systems [3]. Thus, we consider the *Lorenz–Fermi–Pasta–Ulam* (LFPU) experiment.

The motivation for an experiment of this kind is rooted in images of turbulence [4] and in theory of spatially extensive systems containing many interacting elements. For example, in climate dynamics, motions cover many different scales and there are several physical variables that play central roles. One way to unravel some of the intricate dynamics is to visualize the system in terms of interacting, spatially localized, complex subsystems. The LFPU experiment is one of the simplest model problems of this kind.

Alternatively, by building a very complicated system from simpler building blocks, we can manufacture a metaphor for complex natural phenomena and explore the birth of new structures at higher hierarchical order. For example, one of the images in biology is the "integron", the structural unit at one level of a hierarchy that is composed of coupled elements from the level below. In such a structure, the interaction of the elements is at least as important as the dynamics of each element. The LFPU system is such an ensemble of coupled elements, each of which has, by itself, a nontrivial dynamics.

Simple coupled systems have also been advocated as numerical laboratories for studying outstanding issues such as reconstruction and predictability [5–8]. The analogue experiments have exposed many of the inherent problems in more sophisticated studies of these issues. For example, it is evident from studying weakly coupled systems that estimates of the dimension of the attractor underlying the climate are hopelessly inadequate [5]. At the end of the current study we address issues of this general flavour, and especially predictability, in the context of the LFPU lattice. Specifically, we show the failure of reconstruction and the existence of spatial limits to predictability (the "dynamical horizon"). Nevertheless, despite these difficulties with reconstruction and predictability, there are alternatives to the standard methodologies that we briefly explore.

Other applications of coupled nonlinear systems include earthquake models [9,10], theory of friction [11,12], neuroscience [13,14], synchronizing biological populations [15], discrete reaction–diffusion systems [16] and morphology of living organisms [17]. In all these applications, one strings together an ensemble of individual elements that have internal, potentially chaotic dynamics.

Some theoretical studies that are related to the present work include experiments with ensembles of Rössler systems that are coupled locally [18–22], or globally [23,24], and simulations of coupled models of neurons [25–29]. Also, in some regards, the dynamics of the LFPU system is similar to that found for coupled map lattices [30–32].

The emphasis of the previous studies with coupled nonlinear oscillators has been on either the phenomenon of phase synchronization [33], or the occurrence and stability of the fully synchronized state. Though we also discuss issues pertaining to synchronization, this aspect of the problem is not our main focus. Our principal goal is to provide a relatively complete exploration of the LFPU system over a wide range in the strength of the coupling; a range including both collective and disorganized behaviour of the lattice elements. In doing so we retreat from a study describing the range of behaviour over the entire parameter space of the system; such a study is simply too involved. But, in varying the coupling strength, we encounter a very rich array of behaviour.

We also concentrate on systems that are neither too large in number nor too small. That way, our lattices are neither low-order dynamical systems nor extensive systems that essentially reproduce the behaviour of a continuum. In the continuum limit, the LFPU system becomes a set of coupled partial differential equations

(PDEs); the "diffusive Lorenz equations". These equations have been considered previously by Qian and Feng [34] who found globally synchronized solutions and steady states, and by Coullet et al. [35], who studied solutions taking the form of sequences of fronts. Here, we identify features common to the continuum limit, and uncover highly discrete phenomena.

The outline of this paper is as follows. In Section 2 we formulate the LFPU experiment. In Section 3 we describe a set of preliminary initial-value problems that set the stage for the subsequent analysis. That analysis includes a discussion of the stability of the synchronized state (Section 4), the steady equilibria (Section 5) and the time-dependent states that emerge when these equilibria lose stability (Section 6). Finally, we explore *incoherent* lattices (Section 7); that is, lattices at very weak coupling strength where the elements evolve largely independent of one another. Section 8 concludes our study.

2. The system

Our problem surrounds a chain of N coupled Lorenz subsystems each described by the coordinates $\{x_n(t), y_n(t), z_n(t)\}$ for $n = 1, 2, \ldots, N$. We couple the subsystems together in one of the simplest fashions: local, nearest neighbour coupling with a strength measured by the parameter, D. Alternatively, this coupling can be interpreted as a discrete form of diffusive coupling of the three fields. In other words, we solve the equations

$$\dot{x}_n = \sigma(y_n - x_n) + D(x_{n+1} + x_{n-1} - 2x_n), \tag{1}$$

$$\dot{y}_n = r x_n - y_n - x_n z_n + D(y_{n+1} + y_{n-1} - 2y_n), \tag{2}$$

$$\dot{z}_n = y_n x_n - b z_n + D(z_{n+1} + z_{n-1} - 2z_n), \tag{3}$$

for $n = 1, 2, \ldots, N$.

We use periodic boundary conditions: $x_1 = x_{N+1}$ and so on. We refer to n as a spatial, discrete coordinate, and the whole system as the LFPU lattice or chain. In all the computations we report in this paper, we use the standard parameter values, $r = 28$, $\sigma = 10$ and $b = 8/3$.

The coupled system has a continuum limit in which the discrete coordinate n becomes a continuous variable χ, and in which we replace $\{x_n(t), y_n(t), z_n(t)\}$ by $\{\xi(\chi, t), \eta(\chi, t), \zeta(\chi, t)\}$. The continuum fields satisfy the PDEs

$$\begin{aligned} \xi_t &= \sigma(\eta - \xi) + D\xi_{\chi\chi}, \\ \eta_t &= r\xi - \eta - \xi\zeta + D\eta_{\chi\chi}, \\ \zeta_t &= \xi\eta - b\zeta + D\zeta_{\chi\chi}, \end{aligned} \tag{4}$$

subject to periodic boundary conditions, $\xi(\chi, t) = \xi(\chi + N, t)$ and so on.

The equations have the symmetry $x_n \to -x_n$, $y_n \to -y_n$ and $z_n \to z_n$. Hence we may generate other solutions from existing ones on applying this symmetry. For solutions that are "up–down" symmetric, we obtain no new solutions in this way. But there are families of asymmetrical solutions that have "mirror-images" in x_n and y_n. Also, the equations are symmetrical under $n \to N - n$ and $n \to n + j$ for any j (and all n). The first is a reflection symmetry in n and the second is the discrete analogue of the continuous translational symmetry of the PDEs connected to (1)–(3).

3. Preliminary initial-value problems

Before we enter into a detailed exploration of the LFPU system, we describe a set of initial-value calculations that gives a first impression of the richness of the chain dynamics. We select $N = 50$ for illustration and the (small amplitude) initial conditions,

$$\begin{aligned} x_n(0) &= 10^{-3} \sin 1.1(3n - 2), \\ y_n(0) &= 10^{-3} \sin 1.1(3n - 1) \quad \text{and} \\ z_n(0) &= 10^{-3} \sin 3.3n. \end{aligned} \tag{5}$$

Depending on the value of D, we found three types of behaviour for the system evolution:

- Synchronized lattices ($D > 57$).
- Steady, structured lattices ($D < 57$).
- Time-dependent, structured lattices ($D < 5$).

For large values of D, the system relaxes to a spatially homogeneous state. That is, the subsystems synchronize and execute an orbit of the Lorenz equations (see Fig. 1). The convergence to the synchronized state is shown in more detail in Fig. 2. This

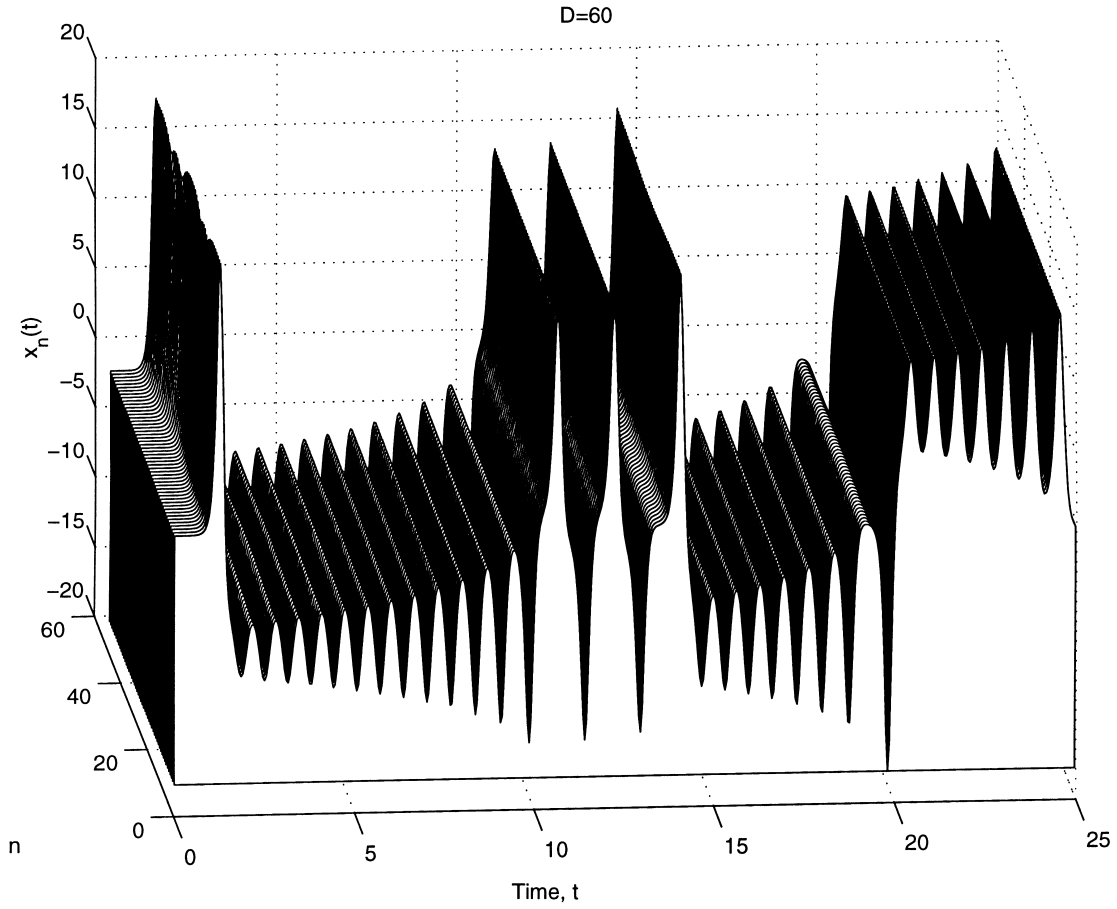

Fig. 1. Synchronized evolution of $x_n(t)$ at $D = 60$.

shows the decay of the sum of squared differences, $\log_{10}\{\sum_{n=1}^{N}[x_n(t) - x_1(t)]^2\}$, which is roughly exponential. The rate of convergence to synchronization decreases with D until $D \approx 57$, where convergence ceases altogether.

For smaller values of D, the subsystems no longer synchronize. Instead, as shown in Fig. 3 for $D = 53$, the systems come close to synchronizing for a while, but then a sudden transition occurs and steady equilibrium states appear. Note that the initial evolution in Fig. 3 leads to a spatially structured state that is almost symmetrical under $n \to N - n$ and reflection. However, there is then a slower phase of evolution in which the state relaxes to an asymmetrical equilibrium. This suggests the initial transition generates a weakly unstable, symmetrical equilibrium, and the final state is a stable asymmetrical equilibrium. The existence of such equilibria is confirmed later.

The loss of stability of the synchronized state is similar to that seen in lower-dimensional systems exhibiting master–slave synchronization [22]. In those systems, an invariant, chaotic set loses stability in a transverse direction (a "blow-out" bifurcation [36]), and the system desynchronizes. An important feature of these systems is that the transverse stability is determined by some complicated average over this set. Hence the transverse stability exponent is much like a Lyapunov exponent and may not be a well-defined function of parameters (see Section 4).

The evolution shown in Fig. 3 illustrates the eventual relaxation to a singly peaked, asymmetrical,

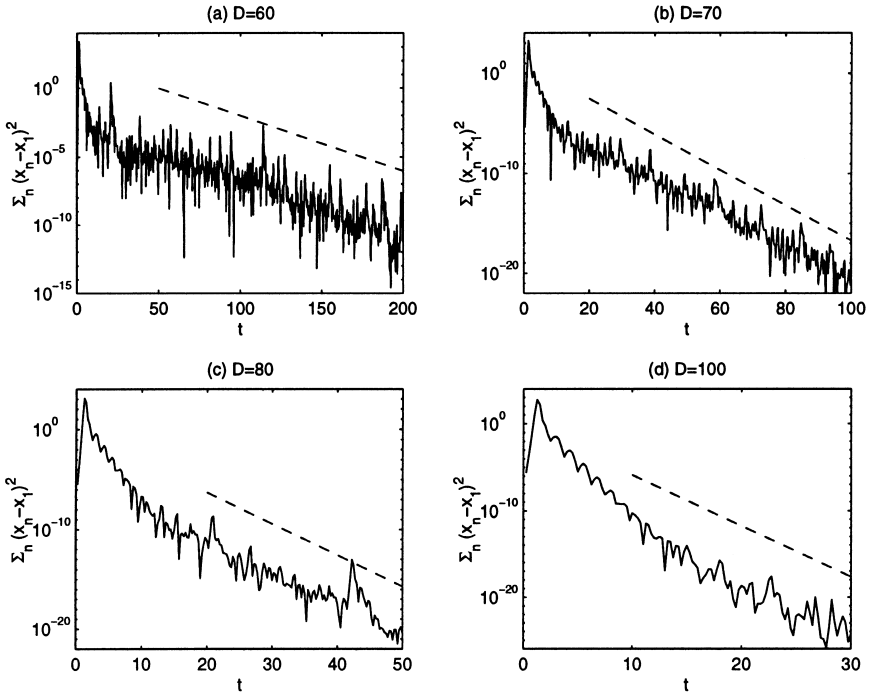

Fig. 2. The convergence of the system to the synchronized state for $D = 60$, 70, 80 and 100. The ordinate is $\sum_{n=1}^{N}[x_n(t) - x_1(t)]^2$. The dotted lines show the rates of convergence estimated from the stability exponent Λ of Section 4.

steady equilibrium.[1] This is typical over the range $20 < D < 57$ (and is similar to the states explored in [29]). However, there are a variety of different kinds of states found by the initial-value calculation. For example, for values of D in the range 5–20, the equilibria generated in the initial-value problem are doubly peaked (Fig. 4a). At yet lower D, steady states can emerge with more complicated structure (Fig. 4d); in these final states, the number of principal peaks increases as we lower D, until we come close to the maximum number of $N/2$ peaks, corresponding to a "zig-zag" solution. We explore the steady states in more detail in Section 5.

Another regime is present at small values of D. Here, the system can evolve to a time-dependent solution. Some of the time-dependent solutions are similar to the steady equilibrium states, save that in the wider regions between the main peaks, low-amplitude oscillations occur (Fig. 4b and c). These oscillations can be periodic or aperiodic; we explore these states in Section 6. Other time-dependent states that emerge at yet smaller coupling strength have no such underlying spatial structure. The dynamics of these states is more like an ensemble of weakly coupled, but individually evolving, chaotic elements. We explore such states in Section 7.

In Fig. 5 we give a crude classification of the end states of the various initial-value computations. In fact, the picture displays much more than the results of these computations; essentially, this figure displays a "regime diagram" of the LFPU system. The significance of the other curves that are shown in the figure is made clear in the following sections. With the reader's indulgence, we will leave a discussion of all the results until Section 8.

The initial-value computations are classified according to the number of principal peaks in the time-averaged spatial structure; we use the scheme S^n and A^n to indicate a solution with n principal peaks, and S

[1] By "peak", we mean large positive or negative excursions of the variable x_n or y_n between zero-crossings, or *principal* peaks.

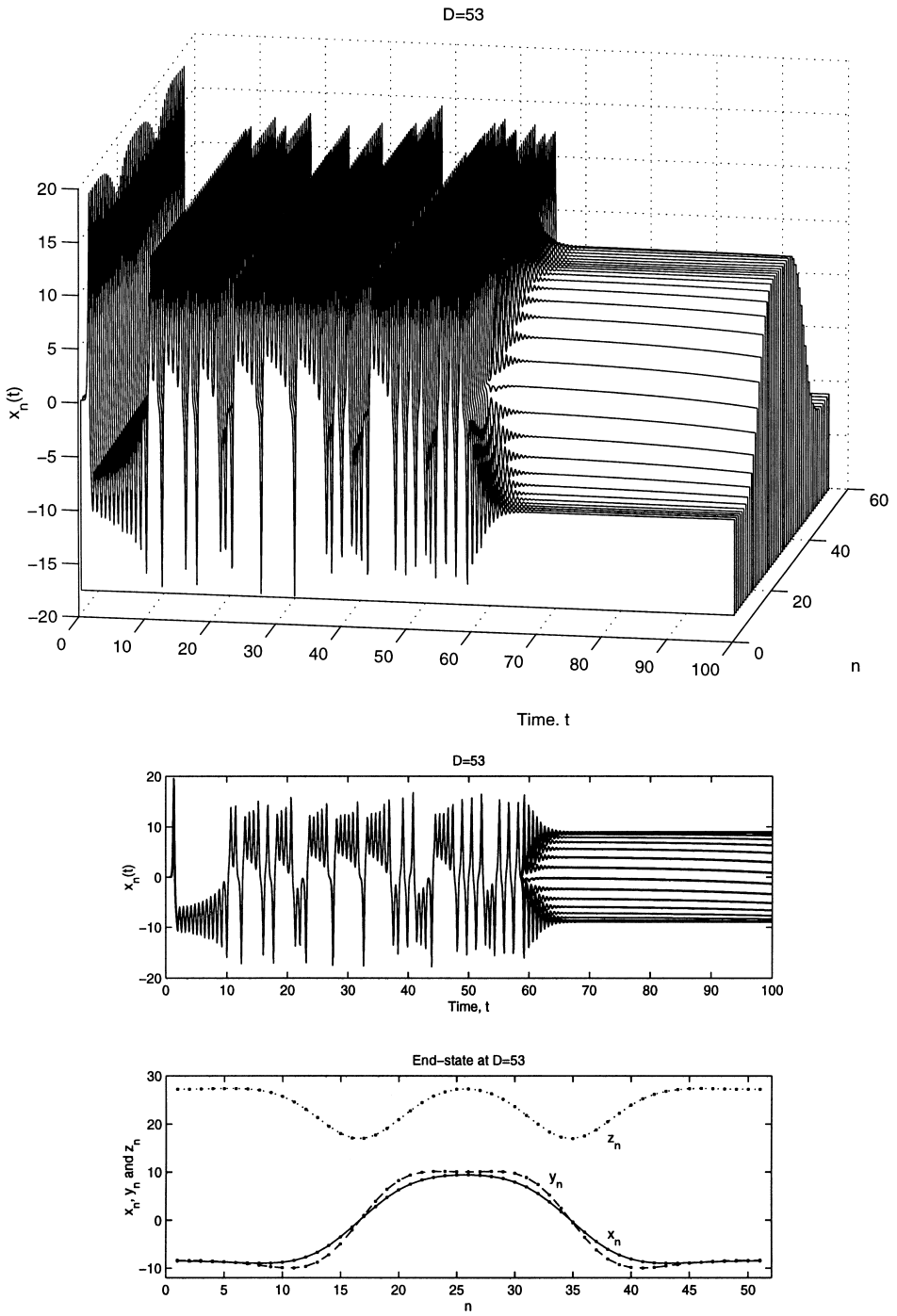

Fig. 3. Initially synchronized evolution of $x_n(t)$ at $D = 53$. Subsequently, at $t \approx 60$, the system shows a sudden transition to an almost steady equilibrium state. Note that the state created by this transition evolves on a much slower timescale from a symmetrical (under $n \to N - n$ and reflection) structure to an asymmetrical one. The final, steady equilibrium state is shown in the lower panel.

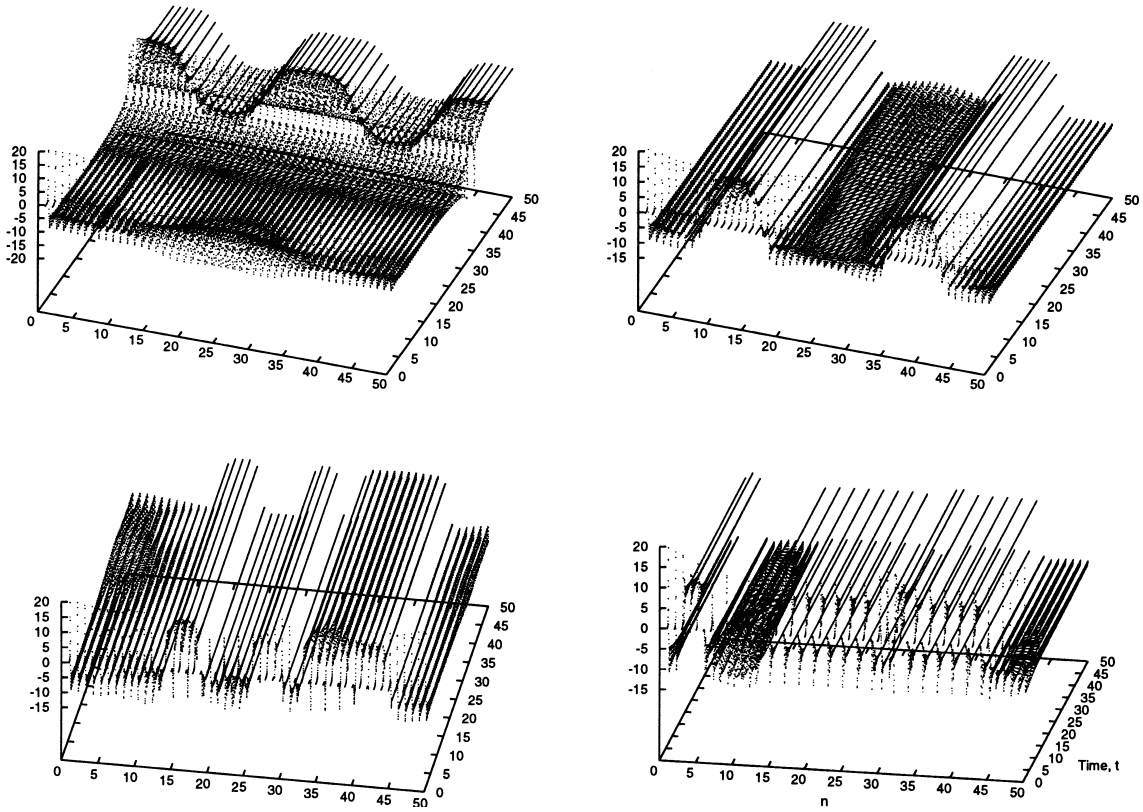

Fig. 4. Initial-value problems at $D = 15$, $D = 3$, $D = 1.5$ and $D = 1$. Shown are values of $x_n(t)$ against n and t at intervals of 0.05. The first and final pictures show states that ultimately becomes steady; there are two and 15 primary peaks in the spatial structures (they are A^2 and A^{15} states in the terminology of Fig. 5). The second and third cases evolve to states that are time dependent with spatially localized oscillations over the widest regions between the main peaks. These final states persist for at least 500 time units, and have two and three main peaks (tA^2 and tA^3 states), respectively.

or A indicate whether the state is symmetric or asymmetric on reflection about $x_n = 0$ ($A^1 \equiv A$ and $S^1 \equiv S$). Note that the time-dependent states are evolved for up to 500 time units and no further; they are not necessarily attractors. In fact, evolution can proceed on much longer timescales (see Sections 6 and 7).

We also add points to Fig. 5 corresponding to initial-value computations for $N = 10$ and 20; these computations were less expensive and we evolved the lattices for longer to be more confident that the end states were attractors.

4. Stability of synchronized states

For large values of D, the system evolves to a spatially homogeneous equilibrium, corresponding to synchronization. This state is given by $(x_n, y_n, z_n) = (X, Y, Z)$, where (X, Y, Z) is a trajectory of the Lorenz system. It is straightforward to show that this state is a solution of the LFPU system for all values of D; that is, it is an invariant manifold in the phase space of the system.

To study the stability of the spatially homogeneous states we set

$$\begin{aligned} x_n(t) &= X(t) + \mathcal{X}(t)\,\mathrm{e}^{2\mathrm{i}\pi kn/N}, \\ y_n(t) &= Y(t) + \mathcal{Y}(t)\,\mathrm{e}^{2\mathrm{i}\pi kn/N}, \\ z_n(t) &= Z(t) + \mathcal{Z}(t)\,\mathrm{e}^{2\mathrm{i}\pi kn/N}, \end{aligned} \tag{6}$$

for $k = 1, 2, \ldots, (N-1)/2$ or $N/2$ (depending on whether N is odd or even). Substitution into the equations then gives the system,

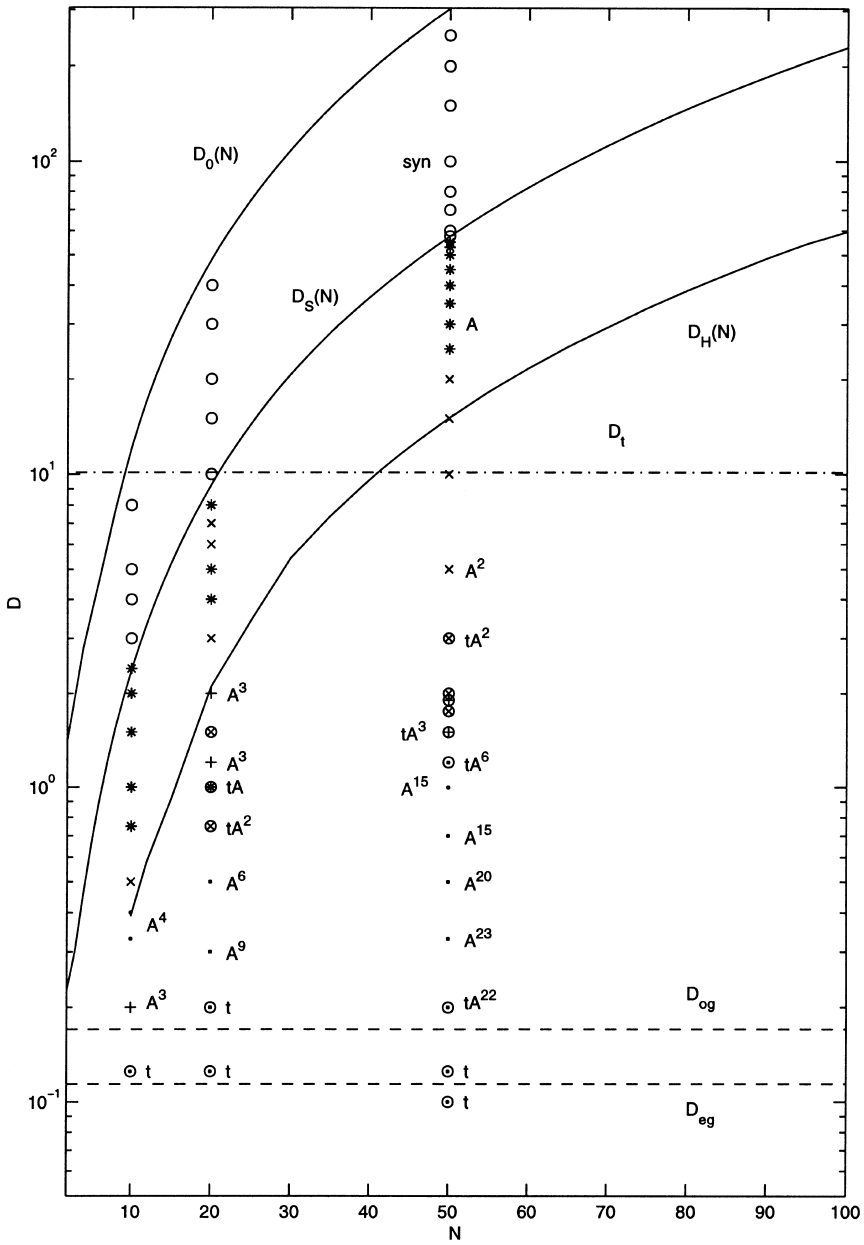

Fig. 5. Regime diagram for the LFPU system. The results of initial-value problems at $N = 10$, 20 and 50 are shown by points with symbology described below. The curves are (i) $D_S(N)$, the stability boundary of the synchronized state; (ii) $D_0(N)$, the upper stability boundary of the symmetrical steady state S; (iii) $D_H(N)$, the Hopf bifurcation along one of the A solution branches (described more fully in Section 5 — it is the A_1 branch, as defined there); (iv) D_{eg}, the lower stability threshold of the even grid mode; (v) D_{og}, the lower stability threshold of the odd grid mode; (vi) $D_t \approx 10.14$, the coupling strength for which the pseudo-translation eigenvalue has magnitude 10^{-3} for the S state. The types of end-states are shown by the symbols plotted at the respective values of D; this classification is based on the number of principal spatial peaks in structured states, and the temporal behaviour. Empty circles indicate synchronized states. Stars are singly peaked steady states (S or A solutions). Crosses are doubly peaked states (denoted A^2 solutions). Plus signs are triply peaked states (denoted A^3). Dots show states with more peaks, A^n. If the state was time dependent, there is a circle around the symbol; thus a circled cross indicates a time-dependent, doubly peaked solution (tA^2). The states at smallest D marked t were time-dependent, had no fixed spatial structure, and identifying principal peaks was ambiguous; these t states may not be attractors.

$$\frac{\mathrm{d}}{\mathrm{d}t}\begin{pmatrix}\mathcal{X}\\ \mathcal{Y}\\ \mathcal{Z}\end{pmatrix} = \mathbf{M}\begin{pmatrix}\mathcal{X}\\ \mathcal{Y}\\ \mathcal{Z}\end{pmatrix} - 4D\sin^2 q\begin{pmatrix}\mathcal{X}\\ \mathcal{Y}\\ \mathcal{Z}\end{pmatrix},$$

$$\mathbf{M} = \begin{pmatrix}-\sigma & \sigma & 0\\ r-Z & -1 & -X\\ Y & X & -b\end{pmatrix} \tag{7}$$

and $q = \pi k/N$. Stability follows from the asymptotic behaviour of $(\mathcal{X}, \mathcal{Y}, \mathcal{Z})$ as $t \to \infty$. In fact, if we let $(\mathcal{X}, \mathcal{Y}, \mathcal{Z}) = (\tilde{\mathcal{X}}, \tilde{\mathcal{Y}}, \tilde{\mathcal{Z}})\exp(-4Dt\sin^2 q)$, then the amplitudes satisfy the system,

$$\frac{\mathrm{d}}{\mathrm{d}t}\begin{pmatrix}\tilde{\mathcal{X}}\\ \tilde{\mathcal{Y}}\\ \tilde{\mathcal{Z}}\end{pmatrix} = \mathbf{M}\begin{pmatrix}\tilde{\mathcal{X}}\\ \tilde{\mathcal{Y}}\\ \tilde{\mathcal{Z}}\end{pmatrix}, \tag{8}$$

which is identical to that used to compute the leading Lyapunov exponent, Λ_0, of the Lorenz equations ($\Lambda_0 \approx 0.9055$ for $r = 28$, $\sigma = 10$ and $b = 8/3$). Hence, $(\tilde{\mathcal{X}}, \tilde{\mathcal{Y}}, \tilde{\mathcal{Z}}) \sim \exp \Lambda_0 t$ as $t \to \infty$. Thus, instability exists if

$$\Lambda(q) = \Lambda_0 - 4D\sin^2 q > 0 \tag{9}$$

[19,37]. This relation reflects the competition between the chaotic separation of neighbouring trajectories (as measured by Λ_0), and diffusive smoothing.

The fact that $\Lambda(0) = \Lambda_0$ is the Lyapunov exponent of the Lorenz equations and therefore positive indicates that there must always be a range of wave numbers for which the homogeneous state is unstable. More precisely, the exponent Λ becomes negative for $4D\sin^2 q \approx 0.9055$. Thus all perturbations with q less than $q_\mathrm{c} = \sin^{-1}\sqrt{0.227/D}$ are unstable. The question of stability then amounts to whether the minimum wave number in the system, given by $k = 1$, falls into this unstable range: $\pi/N < q_\mathrm{c}$. In other words, the state is stable if

$$\frac{\pi}{N} > \sin^{-1}\sqrt{\frac{0.227}{D}}$$

$$\text{or} \quad D > D_\mathrm{S}(N) = \frac{0.227}{\sin^2(\pi/N)}. \tag{10}$$

For $N = 50$, this predicts a critical value of D of 57.42, which is in agreement with estimates based on numerical experiments given earlier. The threshold, $D_\mathrm{S}(N)$, is drawn in Fig. 5. Note, also, that synchronization in the continuum case is unstable to long wavelength perturbations in sufficiently large systems. (See also Ref. [38].)

5. Steady states

Below the synchronization threshold, the lattice acquires a nonhomogeneous spatial structure. In this parameter regime, stable steady states appear.

5.1. Equilibria and their stability

To find the steady states explicitly, we set the right-hand sides of (1)–(3) to zero. Then we obtain the boundary-value difference equations

$$0 = \sigma(\bar{y}_n - \bar{x}_n) + D(\bar{x}_{n+1} + \bar{x}_{n-1} - 2\bar{x}_n), \tag{11}$$

$$0 = r\bar{x}_n - \bar{y}_n - \bar{x}_n\bar{z}_n + D(\bar{y}_{n+1} + \bar{y}_{n-1} - 2\bar{y}_n), \tag{12}$$

$$0 = \bar{y}_n\bar{x}_n - b\bar{z}_n + D(\bar{z}_{n+1} + \bar{z}_{n-1} - 2\bar{z}_n). \tag{13}$$

Solutions to these equations are easily furnished on solving the difference equations by Newton iteration.

For future use, we also quote the continuum version:

$$D\bar{\xi}_{\chi\chi} = \sigma(\bar{\xi} - \bar{\eta}), \quad D\bar{\eta}_{\chi\chi} = \bar{\eta} - r\bar{\xi} + \bar{\xi}\bar{\zeta},$$
$$D\bar{\zeta}_{\chi\chi} = b\bar{\zeta} - \bar{\xi}\bar{\eta}. \tag{14}$$

Some sample equilibrium solutions are shown in Figs. 6–9. Figs. 6 and 7 show a class of symmetrical equilibrium states with a single principal peak, and Fig. 8 shows an asymmetrical version. The end-state of the initial-value calculation shown in Fig. 3 is a member of this latter family. A doubly peaked family is shown in Fig. 9. Related solutions are generated by applying the symmetry operation, $(x_n, y_n, z_n) \to (-x_n, -y_n, z_n)$, or by discretely shifting the solutions across the lattice.

The stability of the steady states is determined by setting

$$x_n = \bar{x}_n + x'_n\,\mathrm{e}^{\lambda t}, \quad y_n = \bar{y}_n + y'_n\,\mathrm{e}^{\lambda t},$$
$$z_n = \bar{z}_n + z'_n\,\mathrm{e}^{\lambda t}, \tag{15}$$

substituting into the governing equations, linearizing in the primed quantities, and then solving the eigenvalue problem,

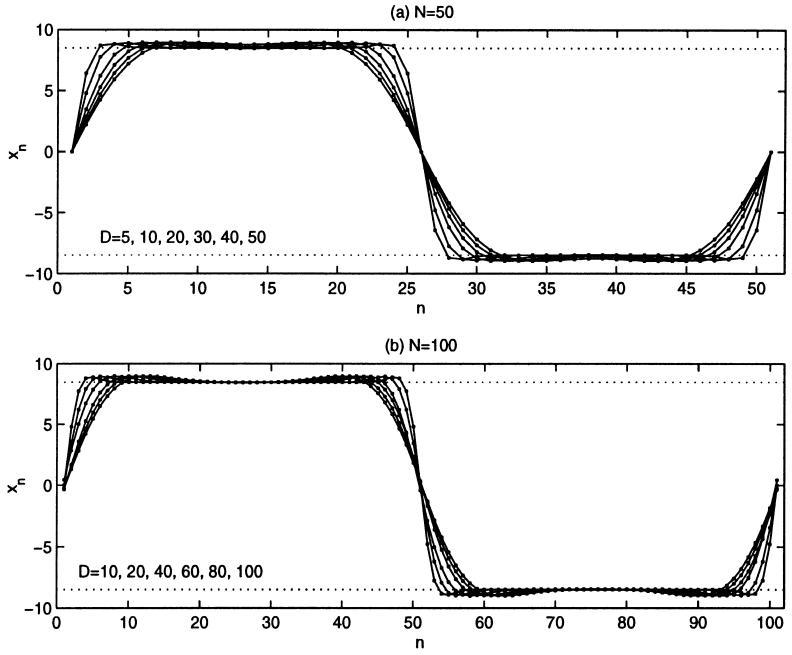

Fig. 6. Steady equilibrium states with a single peak for (a) $N = 50$ and (b) $N = 100$. We denote this state as S. Dotted lines show the value of X at the fixed point of the Lorenz equations. The "steepest" solutions are least strongly coupled.

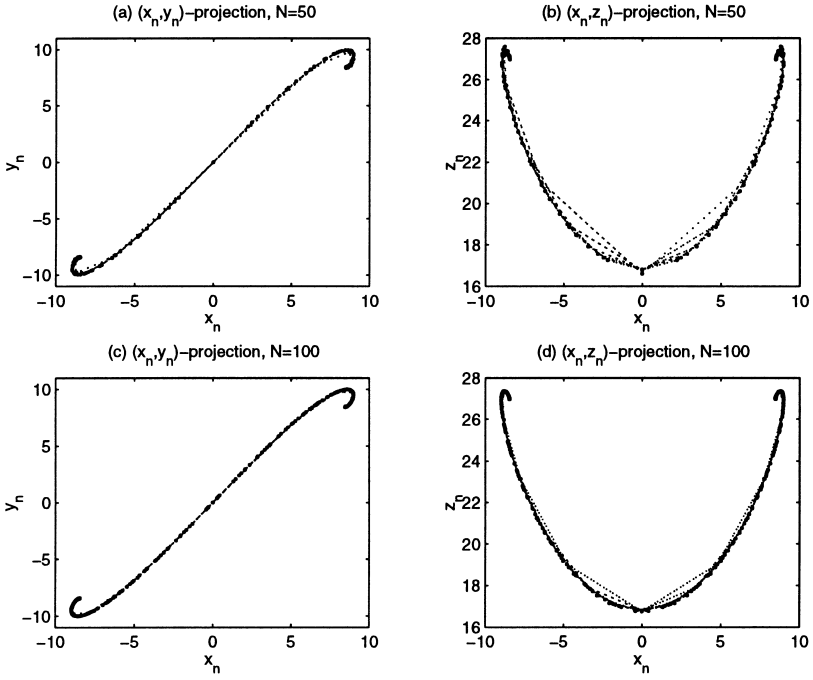

Fig. 7. Steady equilibrium states (as shown in Fig. 6) projected onto the (x_n, y_x) and (x_n, z_n)-planes for $N = 50$ and $N = 100$. Strikingly, the values of x_n, y_n and z_n almost fall on a curve whose shape is independent of N and D.

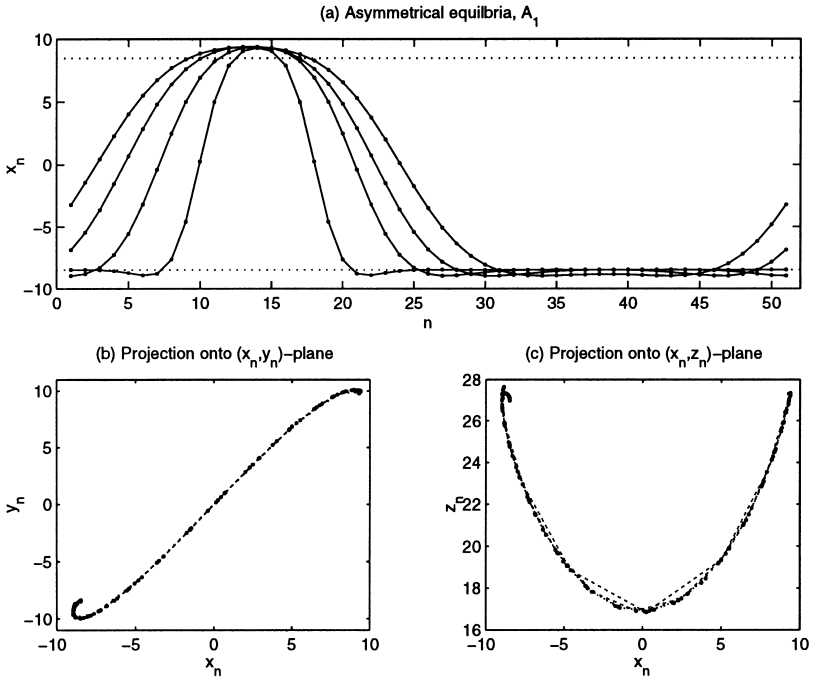

Fig. 8. Asymmetrical steady equilibria at $D = 10$, 30, 50 and 70. This branch of solutions is denoted A_1 and is related to the end-state of the initial-value calculation shown in Fig. 3. There is a "mirror-image" family of solutions with $x_n \to -x_n$, $y_n \to -y_n$ and $z_n \to z_n$. The "smoothest" solutions are most strongly coupled.

$$\lambda x_n' = \sigma(y_n' - x_n') + D(x_{n+1}' + x_{n-1}' - 2x_n'), \tag{16}$$

$$\lambda y_n' = r x_n' - y_n' - \bar{x}_n z_n' - \bar{z}_n x_n' + D(y_{n+1}' + y_{n-1}' - 2y_n'), \tag{17}$$

$$\lambda z_n' = \bar{y}_n x_n' + \bar{x}_n y_n' - b z_n' + D(z_{n+1}' + z_{n-1}' - 2z_n'). \tag{18}$$

Analysis of the stability of the steady states indicates that they remain stable for values of D exceeding the synchronization threshold. Hence, there is a parameter range where both stable synchronization and spatially homogeneous stable steady states are possible attractors. The initial condition (5) used in the initial-value problems evidently favours the synchronized state over this regime.

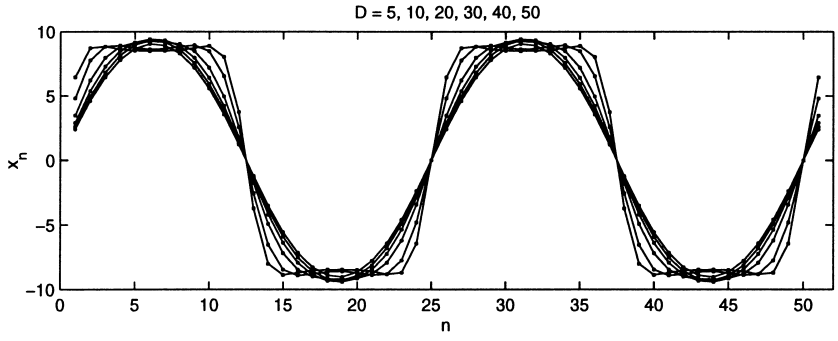

Fig. 9. Symmetrical steady equilibria with two principal peaks; we denote this state as S^2. The "steepest" solutions are least strongly coupled.

5.2. Creation and bifurcations of steady states

The steady states S^k appear by bifurcating from the trivial state, $x_n = y_n = z_n = 0$. (Because of the discrete translational symmetry, this is a highly degenerate bifurcation for a large lattice.) The trivial state $x_n = y_n = z_n = 0$ is actually an unstable, synchronized solution, and so we may apply the stability theory of Section 4 to uncover the location of the bifurcations.

It is straightforward to show that the trivial state has an unstable eigenvalue given by $\lambda_0 = [\sqrt{(1-\sigma)^2 + 4r\sigma} - (1+\sigma)]/2 \approx 11.83$. This eigenvalue corresponds to synchronized perturbations, and so the trivial state is unstable *inside* the "synchronization manifold". But, there is also a *transverse* stability exponent, $\Lambda_0 = \lambda_0 - 4D\sin^2(k\pi/N)$, where k is any integer. This exponent changes sign when $\lambda_0 = 4D\sin^2(k\pi/N)$, or $D \approx 2.96/\sin^2(k\pi/N)$, which is the bifurcation point at which the state, S^k, emerges. The mode of longest scale with $k = 1$ leads to the $S^1 \equiv S$ state shown in Figs. 6 and 7, and the $k = 2$ bifurcation generates the S^2 state shown in Fig. 9.

The bifurcations are pitchforks, and occur at successively lower values of D as k increases. Evidently, there are only as many as $N/2$ independent bifurcations of this kind, with the mode with shortest length-scale emerging at smallest D. For an even lattice, this corresponds to $k = N/2$; when N is odd, the last mode to bifurcate has $k = (N-1)/2$. The resulting $S^{N/2}$ and $S^{(N-1)/2}$ states correspond to the "zig-zag" solutions mentioned earlier.

When the S^k states bifurcate, they share the stability properties of the trivial state at larger D, and so they are all unstable. As we lower the coupling strength, however, further bifurcations occur that stabilize the S^k states. We illustrate this for $k = 1$.

Numerical evaluations of the stability eigenvalues for the single-peaked S^1 solutions of Fig. 6 are displayed in Fig. 10. There are three different kinds of

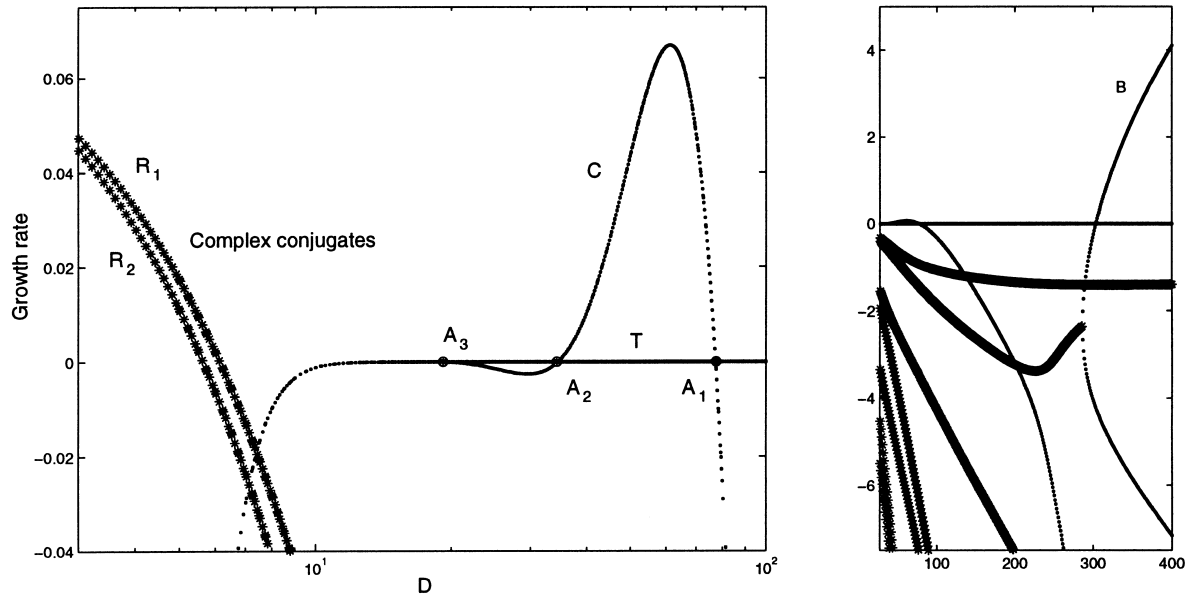

Fig. 10. Stability eigenvalues of the symmetrical states shown in Fig. 6(a). Shown are the real parts of the eigenvalues of largest size; the dots show real modes and stars represent complex conjugate pairs. The real mode labelled C crosses through zero at the bifurcation points of the asymmetrical solution branches $A_1 - -A_3$ shown in Fig. 11. The mode T approximates the translational mode of the continuous system, as described in Section 5.3 (note how this eigenvalue coincides with that of the C mode and becomes negative at small D). The two complex conjugate pairs, R_1 and R_2, destabilize the state at small D; they are examples of "radiative instabilities" which are discussed in Section 6.

instabilities suffered by the state $S \equiv S^1$ that are evident in this figure. First, for large D the mode marked B is unstable (see the right panel of Fig. 10); when the associated eigenvalue passes through zero, the S state first becomes stable. Second, over the range $10 < D < 100$, the C mode "oscillates" several times through zero leading to two bands of instability. Third, conjugate pairs R_1 and R_2 bifurcate to instability at small D. Note that there is another eigenvalue, marked T, with a very small magnitude for $D > 10$. We discuss this mode further in Section 5.3.

A related bifurcation diagram is shown in Fig. 11. The point at which the B mode becomes stable, $D = D_0$ $(N = 50) \approx 303.5$, corresponds to a symmetry-breaking bifurcation where two asymmetrical, single-peaked families of solutions emerge. These solutions are always unstable; we label them

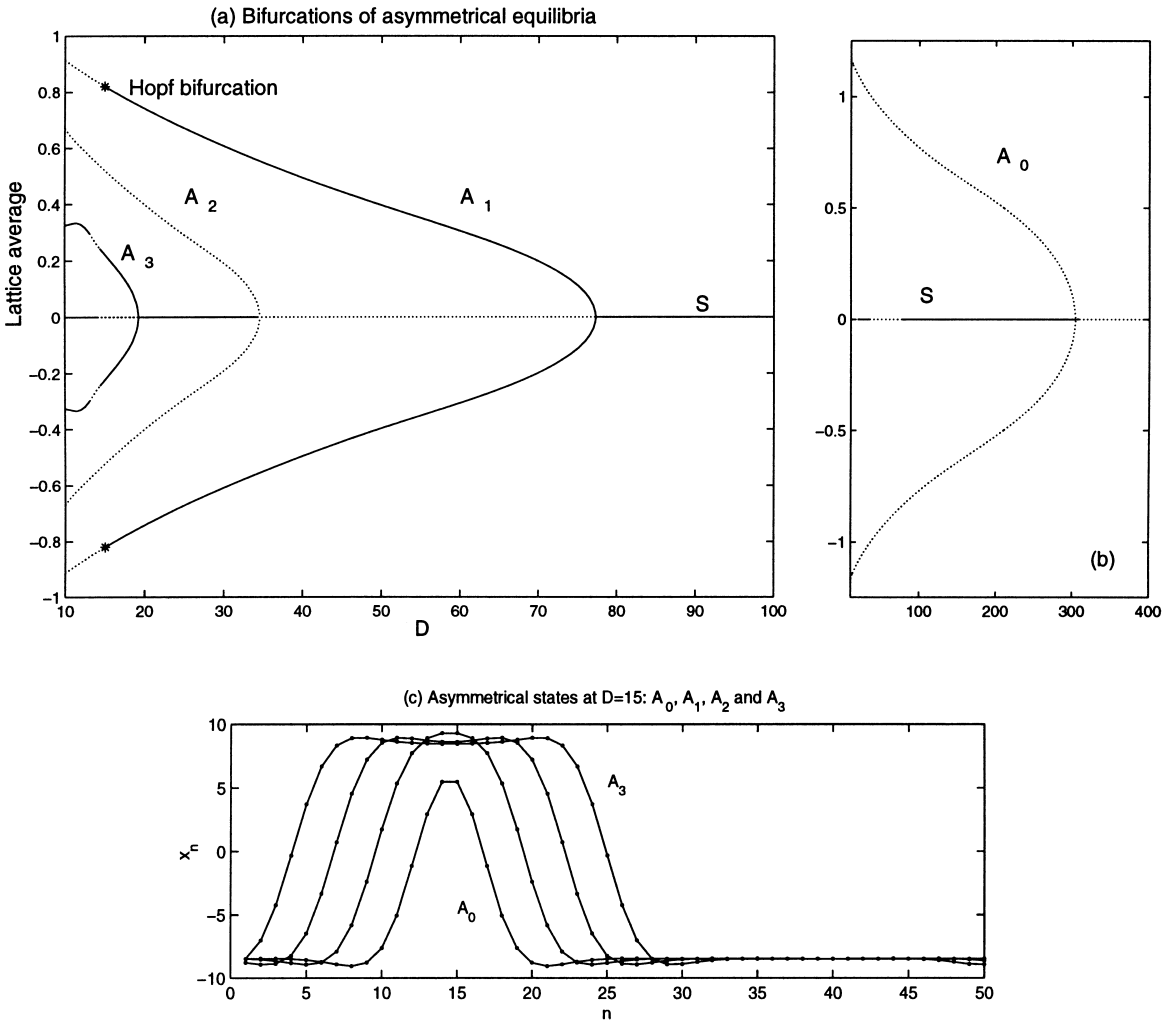

Fig. 11. In panels (a) and (b) we display bifurcation diagrams for asymmetrical equilibria. Shown is the amplitude measure $\sum_{n=1}^{N} x_n/N$ against D. The branch S denotes the symmetrical solutions. Branches shown by dotted lines are unstable. Panel (c) shows the spatial structure of the states, A_0, A_1, A_2 and A_3, at $D = 15$; the "peak" becomes wider on progressing along the branches. The break of stability in the A_3 branch occurs because of a change in the sign of the pseudo-translation eigenvalue. The unstable, symmetrical solution continues to larger D, until $D \approx 1000$ where it bifurcates off the trivial state, $x_n = y_n = z_n = 0$.

as A_0 states.[2] As a result of the bifurcation, the symmetrical solution becomes stable for $D < D_0(N)$. The curve $D_0(N)$ is shown in Fig. 5.

There is a second symmetry-breaking bifurcation at $D \approx 77.5$. Here the symmetrical solution loses stability to another asymmetrical state, the A_1 solution. That solution is the one which is typically observed as the final state in the initial-value computations of Section 3 for $20 < D < 57$. This asymmetrical solution family is also shown in Fig. 8. The solution remains stable down to $D = D_{\rm H} \approx 15$, where there is a Hopf bifurcation (see the star on Fig. 11). This occurs when a complex conjugate pair of eigenmodes becomes unstable, just as the R_1 and R_2 modes destabilize the symmetrical branch S at lower values of D (see Fig. 10). However, the A_1 branch suffers the Hopf bifurcation at relatively large D. The locus of the Hopf bifurcation along the A_1 branch, $D = D_{\rm H}(N)$ is again shown in Fig. 5. The consequences of this oscillatory instability are explored in Section 6.

More symmetry-breaking bifurcations occur on the S branch as we lower D, leading to an interesting pattern in the bifurcation diagram. The symmetrical solutions restabilize near $D = 34.33$ by shedding a second pair of asymmetrical solutions denoted A_2. The next bifurcation generates the stable A_3 solution branch. The fifth bifurcation generates yet another unstable pair of solutions. However, at this coupling strength, the solutions are very discrete and we abandon the A_j classification scheme (cf. Fig. 14 below). The A_0, A_1, A_2 and A_3 solutions are compared in Fig. 11c at $D = 15$. Evidently, as one proceeds from branch to branch, the number of subsystems contained in the "peak" increases.

In addition to the series of bifurcations that occur, the structure of the states also changes in an interesting way as we vary D. For both symmetrical and asymmetrical states, as we decrease D, the equilibrium states become characterized by flat plateaux connected by steep steps (see Figs. 6 and 8). The plateaux lie at the value of the spatially homogeneous, time-independent equilibrium (the nontrivial fixed point of the Lorenz equations): $X = Y = X_{\rm f} = \pm\sqrt{b(r-1)}$ and $Z = Z_{\rm f} = r - 1$. Hence the equilibrium solutions look to be approaching the discrete analogues of heteroclinic connections of the two constant phases or fronts.

5.3. Equilibria near the continuum limit; indiscrete solutions

We rationalize the existence of the mode marked T in Fig. 10 and the apparent approach to "discrete fronts" in terms of the continuum limit. In this limit, the stability problem becomes

$$\begin{aligned}
\lambda\eta' &= \sigma(\eta' - \xi') + D\xi'_{\chi\chi},\\
\lambda\eta' &= r\xi' - \eta' - \bar{\xi}\zeta' - \bar{\zeta}\xi' + D\eta'_{\chi\chi},\\
\lambda\zeta' &= \bar{\eta}\xi' + \bar{\xi}\eta' - b\zeta' + D\zeta'_{\chi\chi},
\end{aligned} \tag{19}$$

where $(\bar{\xi}, \bar{\eta}, \bar{\zeta})$ denotes a equilibrium solution to the continuum equations, and $(\xi', \eta', \zeta')\,{\rm e}^{\lambda t}$ is the infinitesimal perturbation to that state. There is an exact solution to (19) with $\lambda = 0$ and $(\xi', \eta', \zeta') = (\bar{\xi}_\chi, \bar{\eta}_\chi, \bar{\zeta}_\chi)$. This corresponds to the mode associated with the continuous symmetry of translational invariance.

In the discretized system, the translational invariance is broken, and the continuous symmetry is replaced by the discrete version; an integral shift of the solution across the lattice. Nevertheless, provided D is sufficiently large, the system behaves much like the continuous one and there is an analogue of the translation mode, with $\lambda \approx 0$; this is our T mode. However, the eigenvalue is finite; when it is positive, there is a weakly unstable mode corresponding to a drift across the lattice.

In fact, for strong coupling, there are two families of almost identical equilibrium solutions with slightly different distributions along the chain. One family has a stable "pseudo-translation" mode; the other is unstable. Such pairs of modes are illustrated in Fig. 12. One solution corresponds approximately to the shift

[2] Because it turns out that there are many solutions branches with the same number of peaks, the labelling A^l used earlier is not unique. Instead, we use A^l_j, which denotes the unique solution branch, j, with l principal peaks. In particular, the different asymmetrical branches appear at different values of D. We use j to denote these branches in the order that they appear as we lower D. Note also that $A_j \equiv A^1_j$.

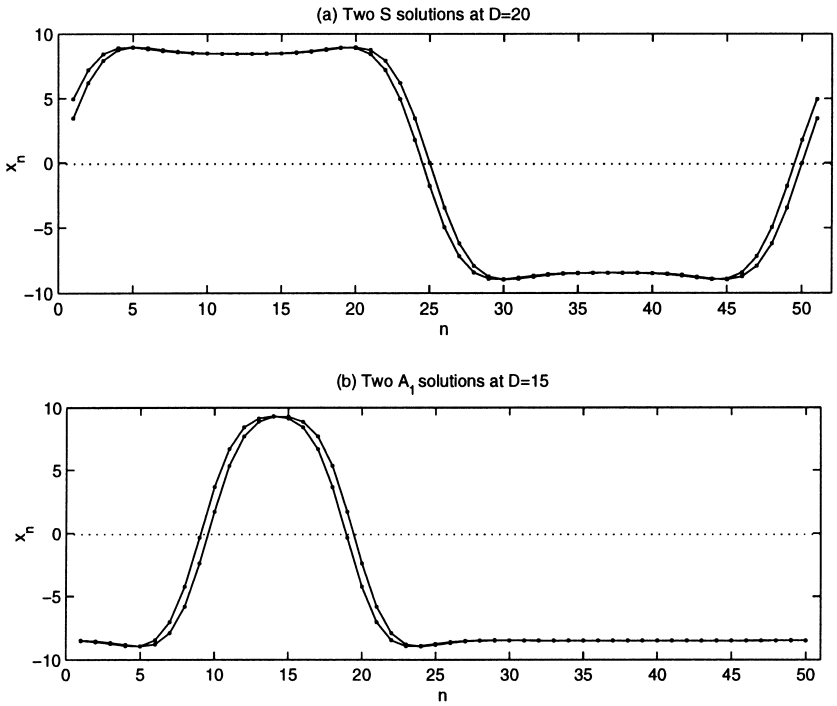

Fig. 12. (a) Two distinct, symmetrical equilibrium states at $D = 20$ that result from the breakage of the continuous translational symmetry in the discrete problem. Both have stability eigenvalues of order 10^{-8}, but one is positive, indicating the state is unstable, and the other negative (indicating stability). In (b), we show a similar pair for the A_1 solution at $D = 15$. The solutions with a subsystem in the vicinity of $x_n = y_n = z_n = 0$ are "centred" and unstable; the "off-centred" solutions are stable.

of the other solution across *half* a lattice spacing. The unstable states correspond to "centred solutions" with a subsystem in the vicinity of $x_n = y_n = z_n = 0$, and the stable equilibria to "off-centre solutions" (see Fig. 12).

In other words, there are two sets of interlaced steady equilibria arrayed across the lattice, one stable and the other unstable. If initialized at the unstable equilibrium, the system subsequently drifts to the stable state. This situation is analogous to that in discrete nonlinear field theories. There, the difference in the energies of the two families provides a potential energy barrier between the neighbouring stable states; this is the so-called Peierls–Nabarro barrier [39].

When D becomes small, the pseudo-translation eigenvalue increases in absolute value reflecting the emergence of effects of discreteness. In fact, the value of this eigenvalue provides us with a measure of how close a particular equilibrium state approximates one in the continuous system (for the symmetrical S states this eigenvalue has magnitude 10^{-3} when $D = D_t \approx 10.14$, once N exceeds about 15; $D = D_t$ is sketched in Fig. 5).

Note that we can rescale the independent coordinate in (14) so as to remove the explicit dependence on D. In other words, the equilibria of the continuous system depend only on the coupling parameter through the scale of n. Thus phase portraits on the (ξ, η) or (ξ, ζ) planes would be independent of D, and the locations for which n were integer would vary along the trajectories. This is essentially what we see in Figs. 7 and 8.

In the continuous system, the heteroclinic connections are solutions to (14). Near the fixed points, we let

$$\bar{\xi} = X_{\rm f} + \tilde{\xi}, \quad \bar{\eta} = X_{\rm f} + \tilde{\eta} \quad \text{and} \quad \bar{\zeta} = Z_{\rm f} + \tilde{\zeta}, \tag{20}$$

and then solve the linear system

$$D\tilde{\xi}_{\chi\chi} = \sigma(\tilde{\xi} - \tilde{\eta}), \quad D\tilde{\eta}_{\chi\chi} = \tilde{\eta} - r\tilde{\xi} + Z_{\rm f}\tilde{\xi} + X_{\rm f}\tilde{\zeta},$$
$$D\tilde{\zeta}_{\chi\chi} = b\tilde{\zeta} - X_{\rm f}(\tilde{\xi} + \tilde{\eta}). \tag{21}$$

This furnishes the eigenvalues of the flow:

$$(\tilde{\xi}, \tilde{\eta}, \tilde{\zeta}) \sim \exp \nu\chi$$
$$\text{with } D\nu^2 = 13.8546 \text{ or } -0.094 \pm 10.1945\text{i} \tag{22}$$

(these are the stability eigenvalues of the nontrivial fixed point in the Lorenz equations). The rate of decay of the front to the left is given by the eigenvalues with positive real part; that to the right by eigenvalues with negative real part. The least rapidly decaying eigenvalues are those generated by the second relation in (22); these eigenvalues are complex and have argument close to $\pi/4$. Thus the front solutions must be characterized by an oscillatory approach to the fixed values, with a decay rate comparable to the oscillation scale. The fact that the tails of the fronts are oscillatory has important implications. In particular, based on the analogy with Shil'nikov theory [40], we therefore anticipate a vast set of solutions of the continuum system containing multiple fronts [41,42].

In fact, the bifurcation diagram of Fig. 11 is very similar to that observed for pulses in Benney's equation [43,44], which can be interpreted in terms of homoclinic dynamics. Differences arise here because the system (14) is reversible (see [45–47]), and because eventually the characteristic thickness of the near-heteroclinic transitions approaches the lattice spacing. Thereafter, the discreteness of the system ruins any parallel with the continuous system (as illustrated by the disappearance of an approximate translation mode in the stability eigenspectra — see Fig. 10).

5.4. Equilibria for small D; highly discrete solutions

The stable steady states that appear at larger coupling strength continue to exist as we proceed to the limit $D \to 0$. But in this limit, we may better analyse such solutions using another approach.

When $D = 0$, we have N uncoupled Lorenz systems. Because for $r = 28$ these systems are all chaotic, we expect that the LFPU lattice is therefore incoherent in this limit. However, we can nevertheless easily construct a multitude of steady equilibria that satisfy (11)–(13) with $D = 0$. The equation implies that each subsystem must be located at one of the three fixed points of the Lorenz equations (which clearly shows why these states are unstable), $(0, 0, 0)$ $(\pm\sqrt{b(r-1)}, \pm\sqrt{b(r-1)}, r-1)$. Hence, we can build an equilibrium by distributing the subsystems at either of these three points. For example, $(\bar{x}_n, \bar{y}_n, \bar{z}_n) = (\pm\sqrt{b(r-1)}, \pm\sqrt{b(r-1)}, r-1)$ and $(\bar{x}_n, \bar{y}_n, \bar{z}_n) = (0, 0, 0)$ comprise three unstable (synchronized) equilibria. However, any permutation of choices from the three fixed points suffices to define an equilibrium at $D = 0$. Though these solutions are all unstable, they are intimately connected to the steady states we observe at stronger coupling.

By way of illustration, we consider $N = 2$. Then we have the states

$$\begin{aligned} &x_1 = \sqrt{b(r-1)}, && x_2 = \sqrt{b(r-1)}, \\ &x_1 = \sqrt{b(r-1)}, && x_2 = -\sqrt{b(r-1)}, \\ &x_1 = \sqrt{b(r-1)}, && x_2 = 0, \\ &x_1 = 0, && x_2 = 0, \end{aligned} \tag{23}$$

and a slew of others obtained from applying the two symmetries of the system, reflection and a shift of the lattice.

Evidently, as N increases, the number of these unstable states rises dramatically. Though they are all unstable at $D = 0$, many of them become stable as a result of Hopf bifurcations as we raise D. This is illustrated in Fig. 13 for $N = 2$, 3 and 4.

Importantly, the first state to become stable as we raise D is invariably the "grid mode". That is, the mode with

$$(x_1, x_2, x_3, x_4, \ldots) = (\sqrt{b(r-1)},$$
$$-\sqrt{b(r-1)}, \sqrt{b(r-1)}, -\sqrt{b(r-1)}, \ldots). \tag{24}$$

For an even lattice, this mode is a perfect zig-zag, and was denoted by the $S^{N/2}$ state above. But when N is odd, there are two lattice points with the same values for x_n and y_n somewhere along the chain. This is the $S^{(N-1)/2}$ state. The "even grid mode" becomes stable for $D = D_{\rm eg} \approx 0.114$, indepen-

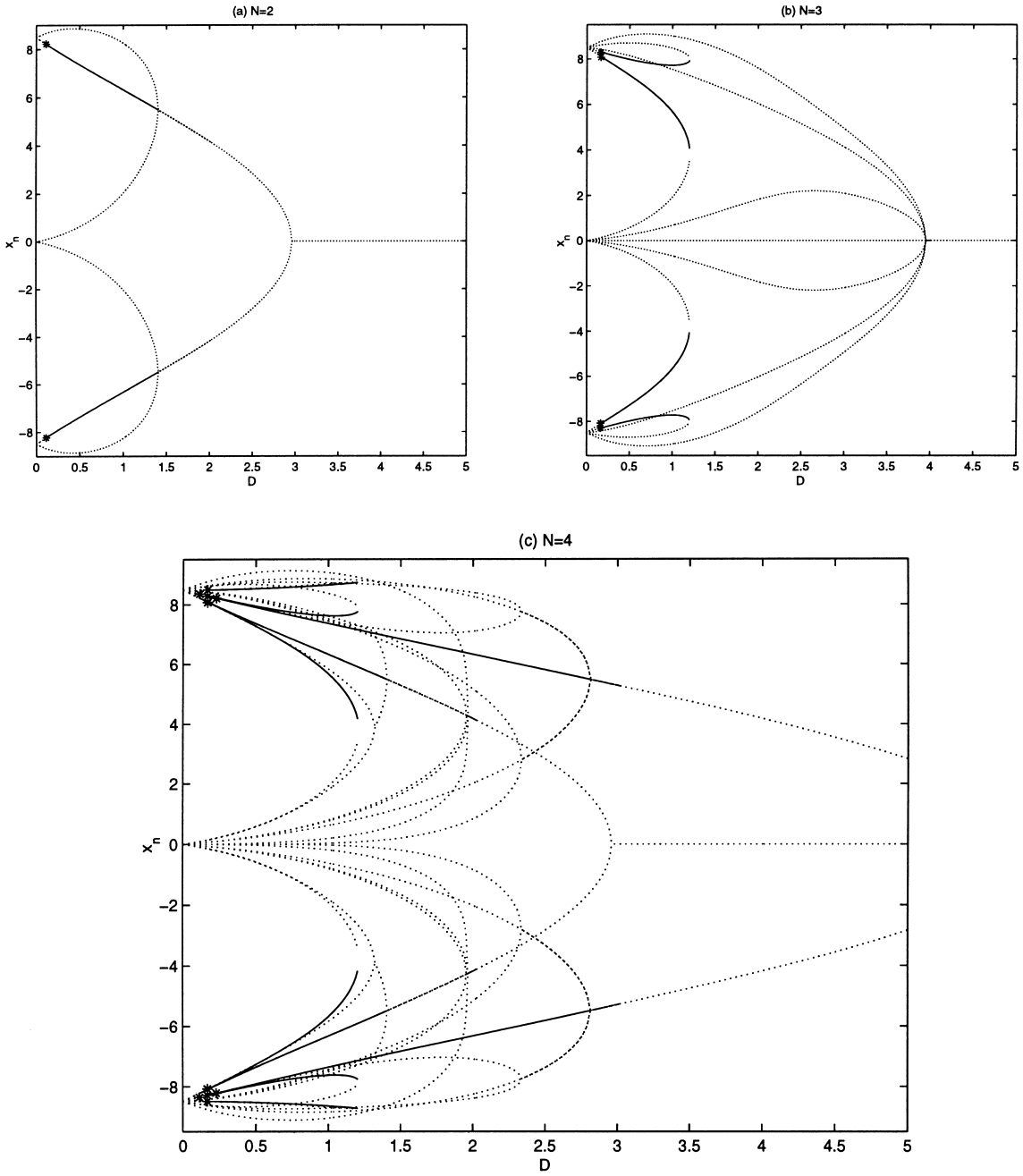

Fig. 13. Bifurcation diagrams of steady states for (a) $N = 2$, (b) $N = 3$ and (c) $N = 4$. The dotted curves denote unstable solutions; solid curves show stable branches. The stars indicate the Hopf bifurcations that stabilize certain of the states at small D.

dent of N. The "odd grid mode" is stabilized as D passes through $D_{\rm og} \approx 0.17$, a number that varies slightly with N. Both $D_{\rm eg}$ and $D_{\rm og}$ are displayed in Fig. 5.

Thus, for large N and small D, we anticipate an exceptionally large number of stable equilibria. Some of these were observed in the initial-value calculations of Section 3. This multiplicity

of states is related to the "attractor crowding" of Weisenfeld and Hadley [48] in coupled map lattices and oscillators. Notably, for $r < 24.7$, where the two nontrivial fixed points are stable, the multitude of stable equilibria extend down to $D = 0$.

Finally, we indicate how the multitude of unstable equilibria at $D = 0$ are related to the equilibrium sequence, S, A_0, A_1, ... We do this by tracing equilibria at $D = 0$ to larger coupling strength for $N = 50$. Results are shown in Fig. 14. This figure shows how equilibria develop on raising D from states given, at $D = 0$, by

$$x_n = \begin{cases} -\sqrt{b(r-1)} & \text{for } n \le j,\ j = 1 \ldots, 25, \\ \sqrt{b(r-1)} & \text{for } n > j,\ j = 1 \ldots, 25, \end{cases} \tag{25}$$

and

$$x_n = \begin{cases} 0 & \text{for } n = 1,\ j = 3, \ldots, 26, \\ -\sqrt{b(r-1)} & \text{for } 1 < n < j,\ j = 3, \ldots, 26, \\ 0 & \text{for } n = j,\ j = 3, \ldots, 26, \\ \sqrt{b(r-1)} & \text{for } n > j,\ j = 3, \ldots, 26. \end{cases} \tag{26}$$

Most of the branches in Fig. 14 terminate in saddle-node bifurcations (we do not trace the unstable branches with which these solutions collide). Two pairs of the solution in panel (a) develop into the A_1 and A_3 solutions, and two pairs in (b) becomes the A_0 and A_2 families. The solutions pair in this way to produce the multiplicity of two in each A_j branch that occurs through the splitting of the pseudo-translation eigenvalue. Similarly, there is a branch in both panels that pair together to become the two symmetrical solutions S.

6. Time-dependent solutions

At intermediate values of D, spatially inhomogeneous, time-dependent states appear. These are related to the Hopf bifurcations that invariably destabilize the equilibrium branches as we lower D.

6.1. Radiative instability for larger N

The fixed-point values that heteroclinic connections approach comprise a spatially homogeneous, time-independent state that is *unstable*. Those fronts

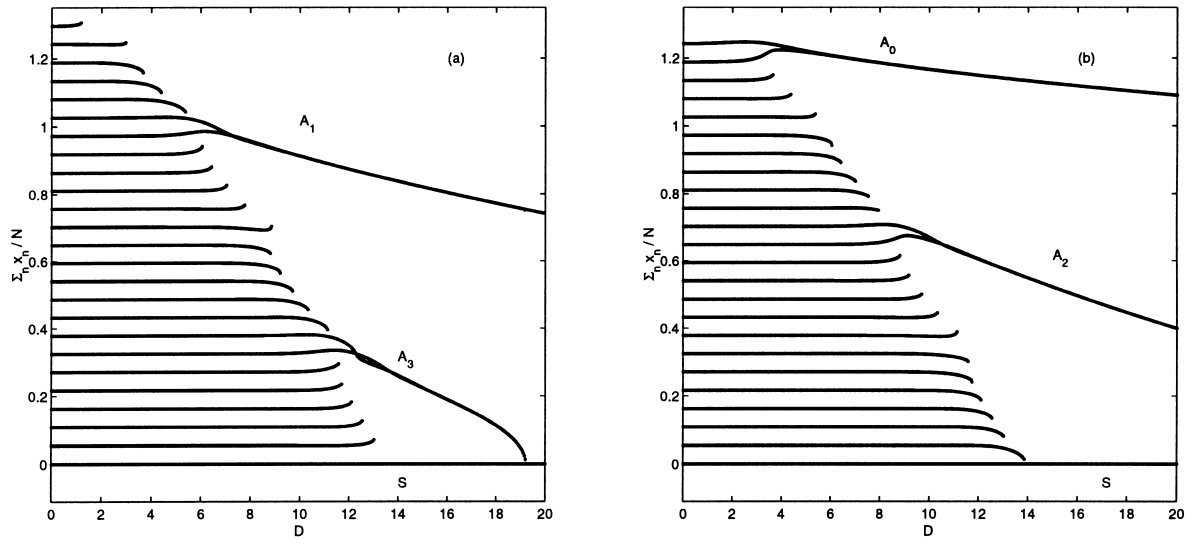

Fig. 14. Bifurcation diagrams of steady states obtained by tracing equilibria at $D = 0$ to larger coupling strength. The two panels indicate the bifurcation curves for the states given in (a) Eq. (25) and (b) Eq. (26). Displayed is the average of x_n over the lattice, $\sum_n x_n/N$.

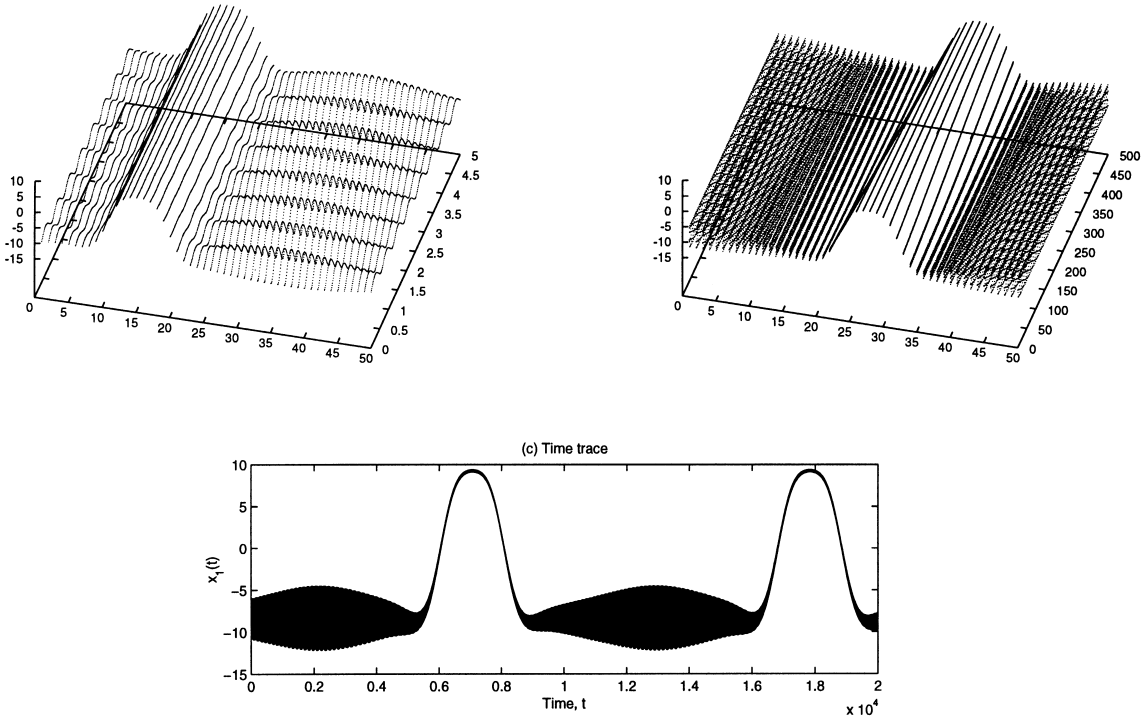

Fig. 15. A detailed view of the time-dependent state at $D = 12$. The panels show successively longer time intervals; the final picture shows the time trace at the first lattice point.

are therefore unlikely to be stable solutions of the PDE in the continuous system: the fronts contain extensive regions over which the amplitudes are essentially no different from the unstable fixed-point values. The situation is again reminiscent of Benney's equation (or even the Kuramoto–Sivashinsky equation), where homoclinic pulses are unstable because the featureless state to which the pulses asymptote is itself unstable [44].

This is the origin of the Hopf bifurcation on the A_1 branch at $D \approx 15$. At this value of D, the state has a sufficiently wide plateau that the equilibrium becomes susceptible to the instability of the spatially homogeneous, time-independent state. These instabilities lead to the time-dependent states at small D that are visible in Fig. 4. In analogy with the terminology of nonlinear field theory, we refer to the instabilities as "radiation" since they are not localized to the fronts and are oscillatory. But when D and N are small, and the system is strongly discrete, this terminology is not useful.

A more detailed view of one of the time-dependent states is given in Fig. 15. This solution corresponds to an unstable A_1 solution, and despite the appearance of the first panel in Fig. 15, is not periodic in time. In fact, the whole spatial structure slowly drifts across the lattice, suggesting that the state is actually a torus. This low drift is presumably the result of the presence of the nearly neutral pseudo-translation mode; the pattern drifts around the chain on timescales of order 10^4, which is what one anticipates based upon the magnitude of that eigenvalue.

The lengthiness of the drift makes systematic studies of time-dependent solutions such as that in Fig. 15 rather laborious. Despite this, we traced this particular solution to both smaller and larger D. The state continues to exist below $D = 9$, and ends in what appears to be a saddle-node bifurcation at $D \approx 16.5$. Because the point of linear stability of the A_1 branch is $D \approx 15$, we conjecture that this Hopf bifurcation is subcritical, that an unstable time-dependent solution

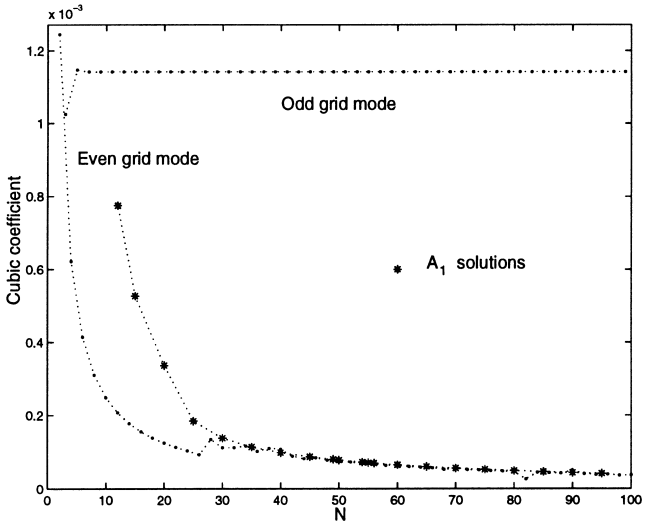

Fig. 16. Landau coefficients at various Hopf bifurcations. Shown are three sets of coefficients corresponding to (i) the Hopf bifurcation at $D \approx 0.114$ for the even grid mode, (ii) that at $D \approx 0.17$ for the odd grid mode, and (iii) the Hopf bifurcation at various $D = D_{\mathrm{H}}(N)$ along the A_1 branch. For larger N, the cases (i) and (iii) lie almost along a common curve despite the fact that the bifurcations occur in different parts of parameter space and for very different equilibria.

emerges, continues to larger D, and then turns around in the saddle node to produce our stable branch.

We confirm part of this speculation by constructing the cubic (Landau) coefficient at the Hopf bifurcation (which is positive, indicating subcriticality). In fact, we have constructed this coefficient at various points on the locus of the Hopf bifurcation along the A_1 branch, $D = D_{\mathrm{H}}(N)$, for the same bifurcation that occurs for the even and odd grid modes (at $D \approx 0.114$ and $D \approx 0.17$, respectively), and for a random selection of other states (such as the S solution) (Fig. 16). The results are always the same; these Hopf bifurcations are invariably subcritical. We conjecture that this criticality is a general property of the LFPU chain for $r = 28$, $\sigma = 10$ and $b = 8/3$. In this sense the lattice behaviour mirrors that of the Lorenz model for which the transition to chaos is through a subcritical Hopf bifurcation.

To make feasible a study of the time-dependent states we retreat to smaller lattices. In particular, we consider systems with $N = 20$. For this lattice size, the time-dependent states occur near $D \approx 1$, where the chain is relatively discrete and there are no pseudo-translation eigenvalues. The states therefore did not drift on long timescales.

The time-dependent state that emerged from the initial-value problem at $D = 1.15$ is shown in Fig. 17. This state is singly periodic for this coupling strength. However, it bifurcates to a torus at larger D, then subsequently back to a limit cycle, as shown by the Poincaré sections of Fig. 18. Those Hopf bifurcations are the only supercritical bifurcations we observed in the LFPU lattice. The branch subsequently ends at $D \approx 3.1$ in what is probably another saddle-node bifurcation. The state to which the solution converges for larger D is an A_1 state that is stable for $D > 2.6$. Thus we conjecture that this state sheds a limit cycle subcritically at $D \approx 2.6$, and this cycle subsequently turns around in the saddle node at $D \approx 3.1$.

The periodic solutions also ends to smaller coupling strength at $D \approx 1.01$. Here, there appears to be a subcritical Hopf bifurcation, and for smaller D, an aperiodic solution develops. A Poincaré section of this solution is shown in Fig. 19. No simple structure is visible in it.

At this stage, we give up. There are too many time-dependent attractors, each with its own sequence of bifurcations, and categorizing them all is simply not feasible. However, the computations highlight that there are time-dependent solutions for small D and

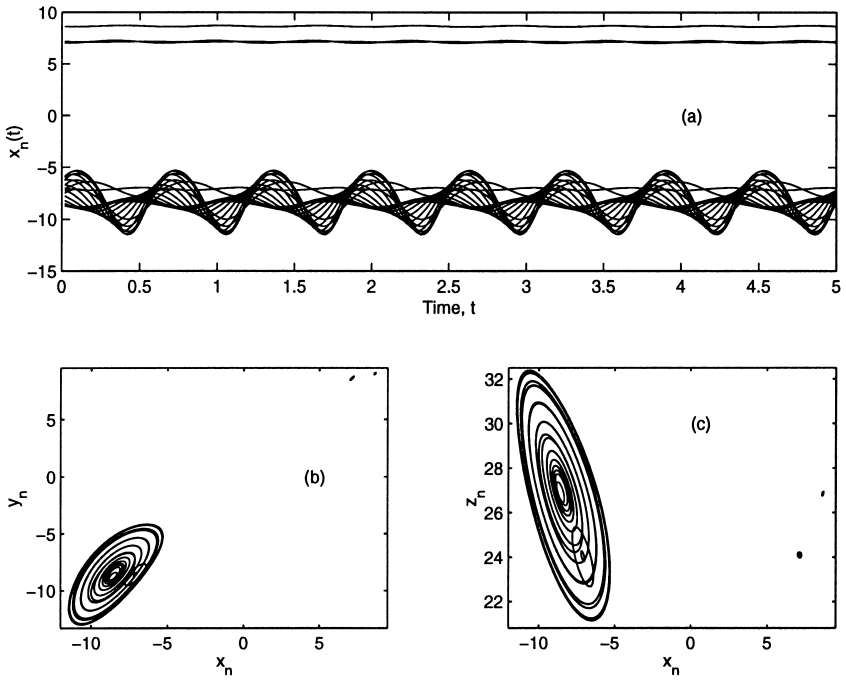

Fig. 17. A time-dependent limit cycle for $N = 20$ and $D = 1.15$. Panel (a) shows a portion of the time series, and (b) and (c) show projections onto the (x_n, y_n) and (x_n, z_n) planes. The plot of the lattice as points above the (n, t) plane is similar to that shown in Fig. 15a. The solution lacks any reflection symmetry of the form, $n \to M - n$, for any (not necessarily integer) M.

larger N. These are all likely to have emerged from limit cycles born in subcritical Hopf bifurcations that subsequently turned around in saddle nodes. Moreover, they can be aperiodic, and probably chaotic.

6.2. Time dependent states for small N; clusters

At small D, the terminology used above is not useful, and one cannot envisage instabilities that are characteristic of wide plateaux in the steady equilibria. Indeed, our preliminary initial-value computations uncovered no similar states for $N = 10$ and smaller; the states marked *t* in Fig. 5 are qualitatively different and have a similar appearance to the incoherent lattices we explore in Section 7 (the subsystems do not have a time-averaged spatial structure that corresponds to some underlying steady equilibrium state). These states may not even be attractors (many of the complicated time-dependent states that we found for $N = 10$ over the range $0.1142 < D < 0.29$ ultimately converged to steady equilibria). However, time-dependent states do exist for lattices with small N. To detect these kinds of states, we make an extensive set of initial-value computations spanning a range of D for $N = 2$, 3 and 4. The results are shown in Fig. 20.

For the two-system lattice, the dynamics can apparently be relatively simply described: for sufficiently large D, the systems synchronize. Then there is a range of D in which the state $x_1 = -x_2$ is a stable, co-existing attractor (this is the even grid mode for $N = 2$); $D_S < D < D_0$. When $D_{eg} < D < D_S$, the synchronized state destabilizes, and the only steady equilibrium is the grid mode. Finally, for $D < D_{eg}$, the lattice is incoherent (see Section 7). Over the range in which the grid mode is stable, but the synchronized state is unstable, there appear to be no attractors other than the steady state; in the initial-value computations, the system always converged to the steady state, although the timescale became longer and longer as $D \to 0.114$ (see Fig. 20).

The absence of any time-dependent attractor for D just above 0.114 (and $N = 2$) suggests that the

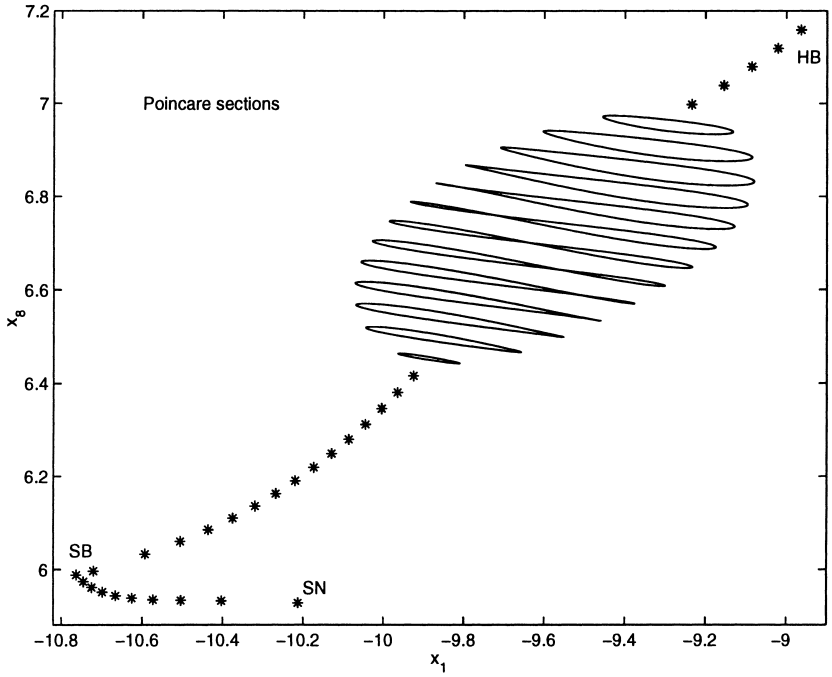

Fig. 18. Poincaré sections for $x_1 = x_2$ projected onto the (x_1, x_8) plane. The solutions shown correspond to $D = 1.05$ to 3.1 in steps of 0.05. The sharp turn to the lower left is due to a symmetry-breaking bifurcation (marked SB in the picture). The solution branch ends in a saddle-node bifurcation (SN) to smaller x_8, and in a subcritical Hopf bifurcation (HB) at larger x_8.

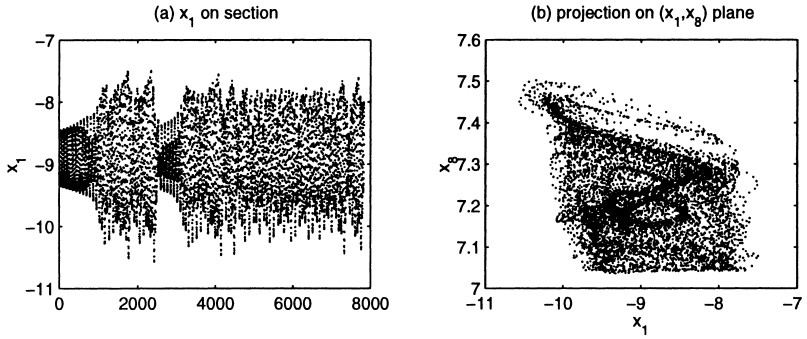

Fig. 19. Poincaré section for $x_1 = x_2$ at $D = 1.004$. Panel (a) shows the sequential values of x_1, (b) the section projected onto the (x_1, x_8) plane.

incoherent state that exists over the range $0 < D < D_{\mathrm{eg}}$ abruptly disappears at that coupling strength. In other words, there is a "phase transition" on the lattice. However, this feature does not persist for larger N. Here, the system does not always converge to a steady equilibrium, but sometimes to a time-dependent state. These solutions consist of states in which the lattice is partitioned into "synchronized clusters" (these are denoted by stars in Fig. 20). In particular, these are states with $(x_2, y_2, z_2) = (x_3, y_3, z_3)$ for $N = 3$, and $(x_1, y_1, z_1) = (x_2, y_2, z_2)$ and $(x_3, y_3, z_3) = (x_4, y_4, z_4)$ in the case $N = 4$. Time series and phase portraits of these states are displayed in Fig. 21.

The clustered states shown in Fig. 21 are not very robust to finite-amplitude perturbations: the introduction of a small difference (of order 10^{-10} or so) into

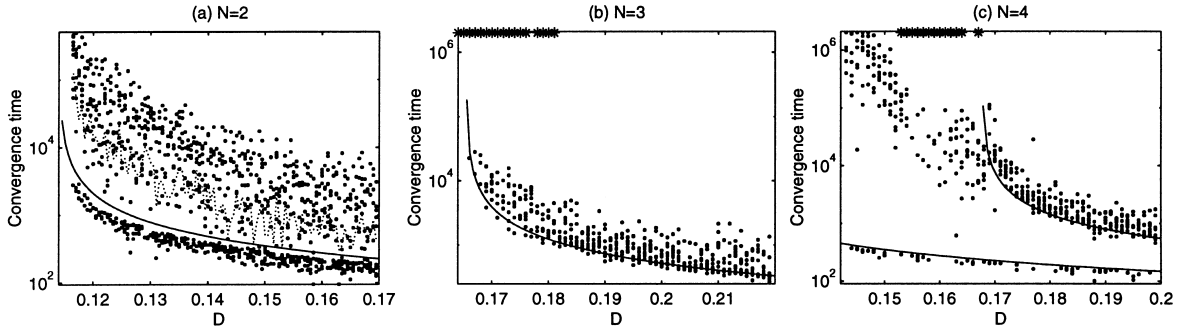

Fig. 20. Convergence time of randomly initialized runs to steady states for $N = 2$, 3 and 4. Ten randomly initialized runs are shown for each value of D. In panel (a), the dotted line shows the logarithmic average of the convergence time; the solid line is an estimate based on the largest stability eigenvalue of the steady states. Similar solid curves are included in panels (b) and (c). The stars in panels (b) and (c) indicate cases in which the system converged to a state in which the subsystems were partitioned into synchronized clusters.

the synchronized coordinates causes the system to diverge from that state on a relatively rapid timescale. None the less, the states appear to be linearly stable attractors (we verified stability numerically by computing Lyapunov exponents). We attribute this feature to the geometry of the phase space near these attractors, which must be unusually complicated [36].

Synchronized clusters are a common feature of globally coupled maps [30–32] and oscillators [24,49]. In those cases, the distribution of the subsystems on the lattice has no special meaning, unlike for our discrete lattice. Consequently, for globally coupled elements, there is a multitude of clustered solutions arising from simple permutations of the lattice index.

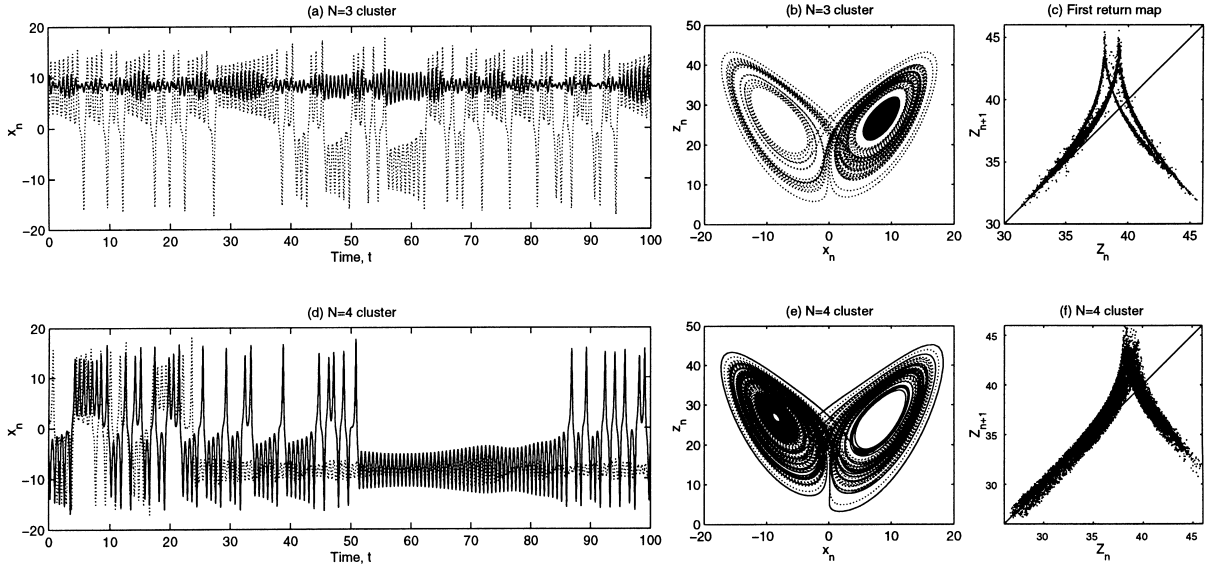

Fig. 21. Solutions partitioned into synchronized clusters. Panels (a)–(c) show a clustered state for $N = 3$ and $D = 0.17$, in which $(x_2, y_2, z_2) = (x_3, y_3, z_3)$ (shown by dotted lines). Panels (d)–(f) show an $N = 4$ state at $D = 0.16$, with $(x_1, y_1, z_1) = (x_2, y_2, z_2)$ and $(x_3, y_3, z_3) = (x_4, y_4, z_4)$. Panel (c) shows a first return "map" of z_2 on the section $\dot{z}_2 = 0$ ($\ddot{z}_2 < 0$), and (f) the return "maps" of z_j on the sections $\dot{z}_j = 0$ ($\ddot{z}_j < 0$), for $j = 1$ and 3 (both are included because the clusters are symmetrical; although these objects are clearly not one-dimensional, we refer to them as maps).

With local coupling, however, arbitrary permutations of the index of the subsystems on the lattice (n) do not generate related solutions, and there is a much smaller set of clustered solutions.

The grid solution is a very special clustered state, as are some of the steady states considered earlier. Indeed, just as we built coupled equilibrium states by continuing uncoupled solutions to larger D, we could also, in principle, perform a similar computation for general clustered solutions. This way we could explicitly construct periodic and chaotic clusters with finite D. The examples shown in Fig. 21 are probably chaotic (their numerically computed leading Lyapunov exponents are positive). In fact, as the return maps indicate, their structure is similar to weakly perturbed Lorenz systems (the case $N = 3$ looks very similar to a perturbed Lorenz model considered in [50]). The $N = 3$ solutions persist over the range $0.138 < D < 0.267$. Other (stable) clustered states that we constructed for larger D were periodic and quasi-periodic. However, we found only a small number of these types of solutions in the initial-value computations shown in Fig. 20, and none in the preliminary initial-value computations reported in Section 3. Thus, time-dependent clustered solutions must have relatively small basins of attraction.

7. Incoherent lattices

When $D < D_{\rm eg}$ or $D < D_{\rm og}$, for even or odd lattices, respectively, there are no more stable steady states embedded in the phase space. At this stage, we conjecture that the dynamics of each subsystem in the lattice is chaotic and the ultimate state shows no spatial coherence. Examples are shown in Fig. 22 for $N = 2$, 3 and 10; two lattices for $N = 50$ are displayed in a different way in Fig. 23.

In Fig. 22, the lattice is initialized with random initial values. The appearance of the time series is much the same for all N, as illustrated by the three panels of the picture. Hence, the dynamics of any one subsystem is largely independent of the size of the lattice. Our computations of measures of complexity, described shortly, go some way to quantifying this feature, and also confirm that the states are chaotic. In other words, for these values of D, we truly enter the regime of weak coupling. We refer to the states shown in Fig. 22 as "incoherent".

Fig. 23 shows evolution from the initial condition in (5). In this second instance, there is a rapid transition to a state that is almost a grid mode. But the zig-zag has "defects" near $n = 1$, 10 and 30, which appear because of the spatial structure of the initial conditions. These defects consist of fully chaotic subsystems. Slowly, these defects expand into the meta-stable zig-zag pattern as subsystems gradually evaporate into the chaotic phase. Eventually, by $t \approx 750$ in Fig. 23a and $t \approx 2000$ in Fig. 23b, the zig-zag pattern completely disappears.

After initial transients of this kind, what we essentially see in Figs. 22 and 23 is the vacillation of the subsystems as they evolve erratically for periods, then become briefly caught in a more coherent phase near what appear to be fixed points, $x_n = \pm x_{\rm p} \approx \pm 8.40$ (and with corresponding values, $y_n = y_{\rm p}$ and $z_n = z_{\rm p}$). In fact, a more detailed examination of the running average of x_n shows that these are not the fixed points of the Lorenz equations ($X_{\rm f} = \pm\sqrt{b(r-1)} \approx \pm 8.49$); we suggest how these coherent phases come about in Section 7.1.

It is interesting that once the initial zig-zag pattern has evaporated, such states rarely reappear spanning more than two neighbouring lattice sites. The main features in Figs. 22 and 23 are briefly coherent episodes, wherein several neighbouring subsystems converge to either $x_n = x_{\rm p}$ (the dark areas) or $x_n = -x_{\rm p}$ (the white areas). That is, briefly coherent, synchronized "blocks" appear sporadically.

Figs. 22 and 23 also indicate that the subsystems wander over extensive portions of phase space. This suggests that as soon as the steady grid solution becomes stable for $D = D_{\rm eg}$ or $D = D_{\rm og}$, the lattice may ultimately fall into that state after exploring a very long transient. Alternatively, the system may eventually converge to a cluster state. However, there are no signs of convergence in Fig. 23b (there is no reappearance of "local" grid modes), suggesting that this lattice may remain incoherent.

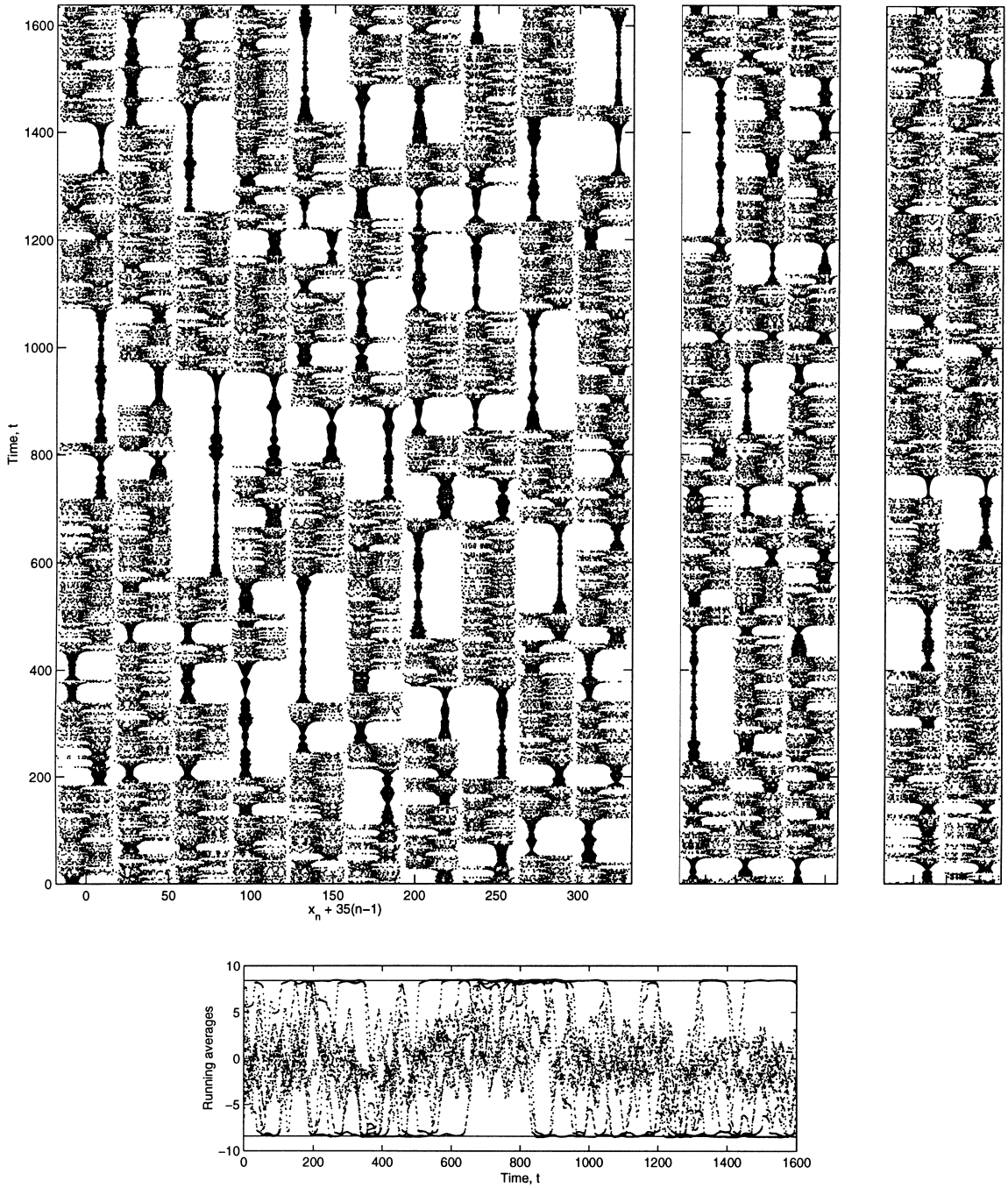

Fig. 22. An incoherent lattice at $D = 0.1$ and $N = 10$. The second two panels show similar results for $N = 3$ and $N = 2$. Initial conditions are random. The final picture shows running averages (over 20 time units) of the solutions shown in the first panel; horizontal lines indicate the estimate $\pm x_p$ in (28).

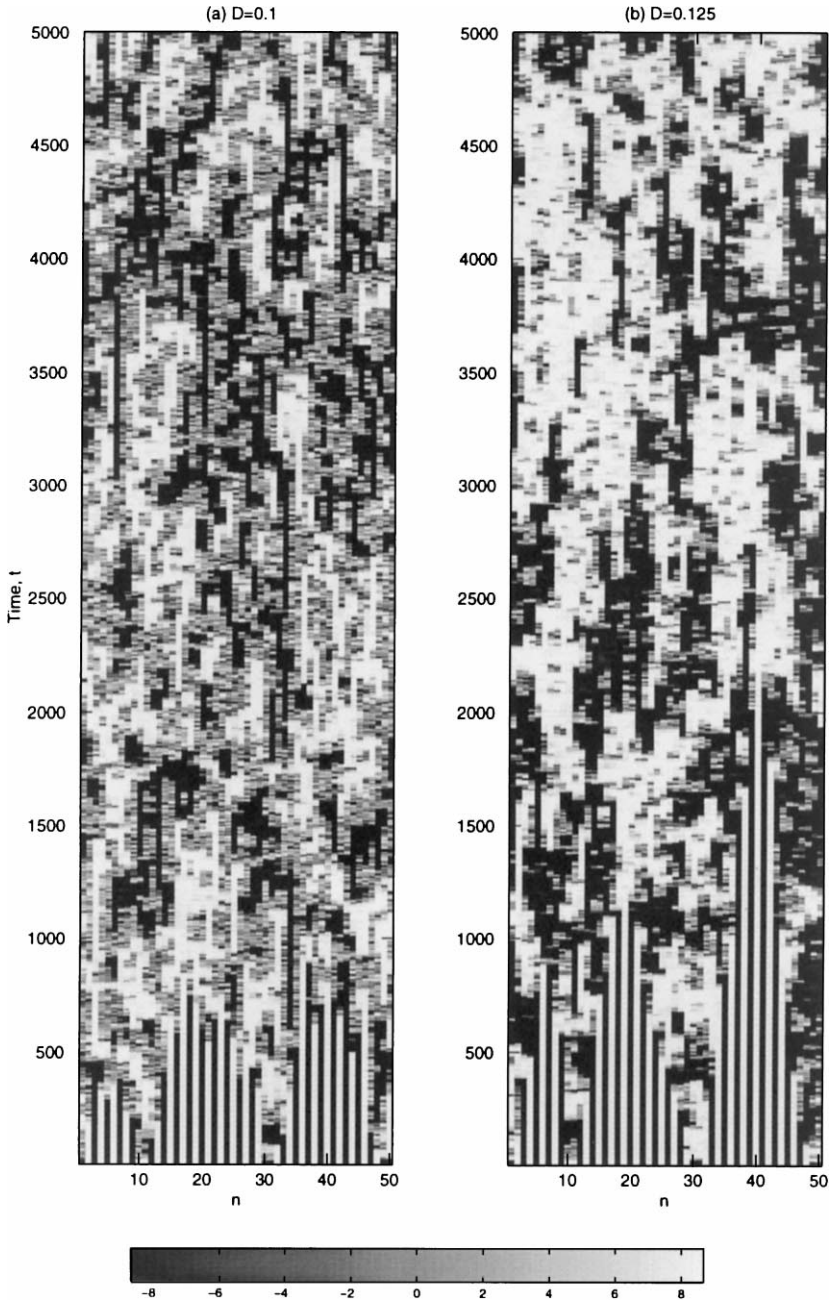

Fig. 23. Incoherent lattices for $N = 50$. Panel (a) shows $D = 0.1$ and (b) shows $D = 0.125$. Shaded is the running average of x_n (over 5 time units) with shading corresponding to level as shown in the key. Initial conditions are given by Eq. (5).

But to resolve the question of whether this state is a very long transient or an attractor, it may take prohibitively long computations, and we leave the question open.

7.1. Coherent phases

During a coherent phase, an individual Lorenz system persists in a stationary state for times much

longer than the intrinsic timescale of variability in the Lorenz equations (the coherent states persist for times of order 10^2, whereas the time for the Lorenz model to complete a circuit of one of the "butterfly wings" is less than 1). As a working hypothesis, we suppose that when one of the subsystems falls into such a state, it is predominantly affected only by the average properties of the two neighbouring, incoherent systems. Hence, because $\langle x\rangle = \langle y\rangle = 0$ and $\langle z\rangle = z_s \approx 23.61$, where $\langle\cdots\rangle$ indicates a temporal average (as given by the Lorenz equations), the coherent subsystem satisfies

$$\dot{x} = \sigma(y-x) - 2Dx, \quad \dot{y} = rx - y - xz - 2Dy,$$
$$\dot{z} = xy - bz - 2Dz + 2Dz_s. \tag{27}$$

That is, the Lorenz equations, but driven by $2Dz_s$, and additionally damped by the "diagonal" coupling terms, $(-2Dx, -2Dy, -2Dz)^T$. This system has fixed points with

$$x = \pm x_p = \pm\frac{\sqrt{[\sigma r-(1+2D)(\sigma+2D)](b+2D)-2\sigma Dz_s}}{\sqrt{\sigma+2D}} \approx \pm 8.4037 \tag{28}$$

(together with corresponding values for y and z), a value that agrees with the running averages of x_n (see Fig. 22). Note that if neighbouring states happen to fall into coherent phases for comparable intervals, similar arguments can be used to furnish the approximate fixed point of the block; the resulting values of x_n are little different.

The stability of the fixed point of the coherent system can also be computed from (27). For $D = 0.1$, the fixed point has a leading stability eigenvalue of -0.0545 ± 10.09i. That is, it is *stable*, which lends some support to the idea that this state can persist for long times. The eigenvalue increases as we lower D, and passes through zero for $D \approx 0.0633$. This suggests that there is a transition in behaviour near this coupling strength.

We explore this possibility further by computing the lengths of the coherent phases as a function of D. More specifically, we measure the lengths of the intervals between the zero-crossings of x_n (see Fig. 24). Roughly speaking, this measurement detects how long each subsystem spends circulating around one of the "butterfly wings" of the Lorenz model; in the coherent phases, the circulation time is substantially prolonged. However, the measurement also contains a characteristic signature of the uncoupled subsystems. This signature is namely the curious, "quantized" structure to the distribution of intervals portrayed in Fig. 24. It arises because the circulations around each focus of the butterfly wings are almost integral in number, and persists for coupled systems with $D < D_{eg}$.

For uncoupled systems, there is a maximum duration to the circulation around a single wing once the trajectory is on the attractor. For the Lorenz model, the maximum duration $\tau_{max} \approx 16.15$. Any interval between zero-crossings that exceeds this maximum time must arise due to coupling, and we identify that interval as a coherent phase. A slight difficulty with this interpretation is that as D varies, each individual subsystem tends to circulate longer purely as a result of the "diagonal" parts of the coupling terms. We remove this effect by taking a Lorenz model and explicitly adding the diagonal coupling terms, then computing a modified maximum circulation time, $\tau_{max}(D)$. As the fixed points become stable in this modified Lorenz model when D is larger than 0.1, we cannot continue to use this estimate for larger coupling strength. Instead, for $D > 0.1$, we use $\tau_{max}(0.1) \approx 32.57$.

The durations of the coherent phases for varying D are illustrated in Fig. 25. The typical duration increases with D until $D \approx 0.085$ where the lengths of the coherent phases appear to be largest (though this is not reflected in the mean values). There is no sudden transition near $D \approx 0.065$ as predicted by the mean model described above, although this coupling strength lies approximately midway between the onset of the coherent phases and where the mean value levels off. As also illustrated in this figure, the coherent phases always appear to be of finite duration. Thus they appear to be only transient states; we never observed an incoherent lattice with a persistent coherent subsystem.

Evidently, coherent phases can be exceptionally prolonged. One consequence of this feature of the lattice dynamics is that it makes the computation of

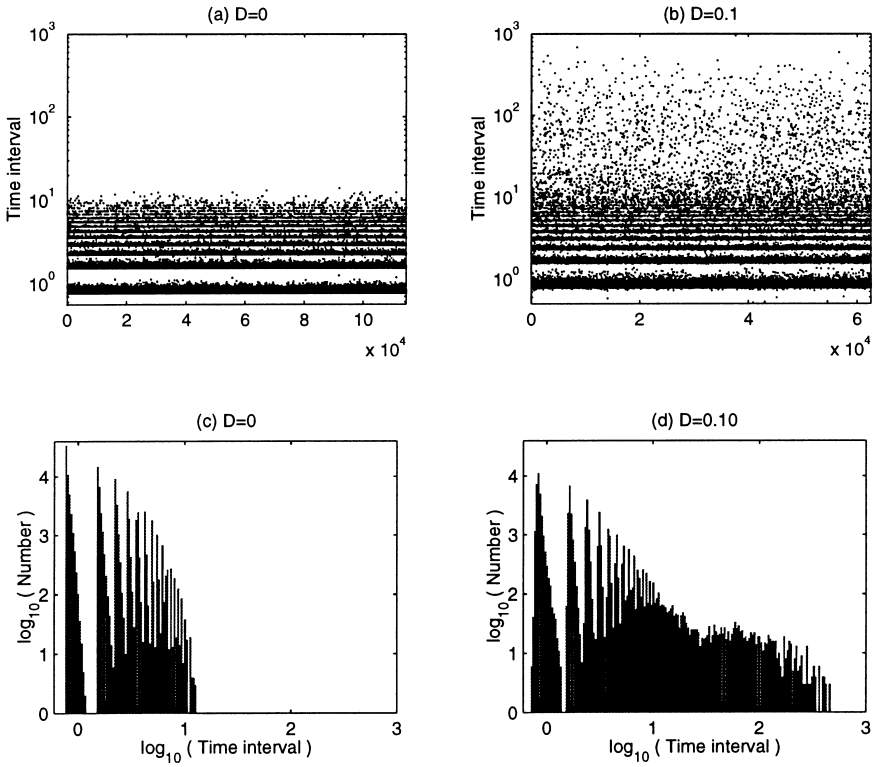

Fig. 24. The intervals between the zero crossings of x_n for a lattice with $N = 10$. Shown in panels (a) and (b) are the intervals plotted in the succession that they were observed. In panels (c) and (d), these intervals are binned and the number of occurrences of an interval inside a particular bin is plotted as a histogram. The cases $D = 0$ and $D = 0.1$ are shown. The duration of the computations was 2×10^4 (all lattice sites are included). Panel (d) suggests that there may be a bi-modal distribution in the zero-crossing times.

statistical measures (as we attempt shortly) an intensive exercise. The presence of coherent phases also leads to particularly long-lived transients. This is basically the origin of the difficulty in identifying attractors for $D \sim 0.1$. For this reason, we do not display result for $D > 0.1142$.

Nevertheless, for $D > 0.1142$, the coherent phases continue to occur. In fact, for such values of D, the

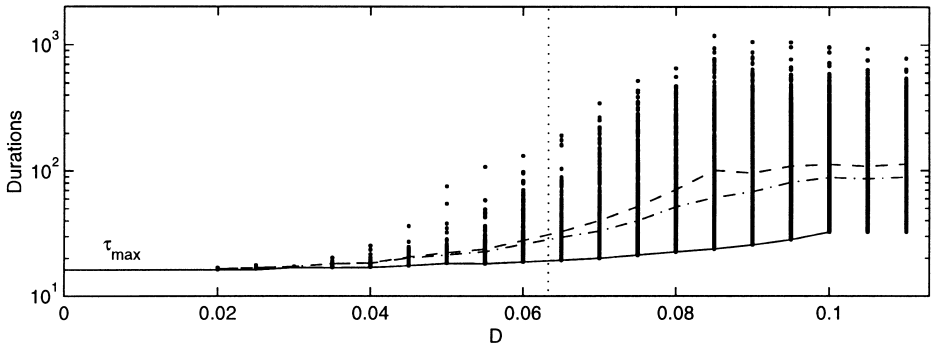

Fig. 25. Durations of coherent phases as a function of D for $N = 10$. The points indicate the durations of phases during a long initial-value computation (of length 2×10^4). The dashed line shows the mean duration and the dot-dashed line the logarithmic average. The solid line is the maximum circulation time for an isolated subsystem, $\tau_{\max}$. The vertical dotted line shows the value of D for which the fixed point of the mean model subsystem (27) loses stability.

phases are clearly associated with intermittent events wherein the system spends an extended period of time near an invariant object in the phase space. For example, with $N = 3$, the coherent phases are associated with intermittent events of full synchronization, or with periods in which the system hovers close a cluster solution of the kind described in Section 6.2. During both events, at least one of the subsystems becomes entrained into a coherent phase (some evidence of this behaviour can already be seen in the second panel of Fig. 22). In other words, at larger D, the alternation between coherent phases and chaotic evolution can be identified as a form of on–off intermittency [51].

As mentioned at the beginning of this section, our explanation of the emergence of coherent phases hinges on the idea that the dominant effect of the coupling for small D is through the driving of one subsystem by the mean z-effect of its two neighbours, and the extra dissipation provided by the diagonal coupling terms. Shorter timescale fluctuations and the reaction of the coherent subsystem on its neighbours are assumed not to be important To gauge whether this is the case we consider a "passive subsystem"; that is, a Lorenz system with the extra dissipative terms and driven by two other Lorenz systems:

$$\begin{aligned}
\dot{x}_2 &= \sigma(y_2 - x_2) + D(x_3 + x_1 - 2x_2),\\
\dot{y}_2 &= rx_2 - y_2 - x_2 z_2 + D(y_3 + y_1 - 2y_2),\\
\dot{z}_2 &= x_2 y_2 - bz_2 + D(z_3 + z_1 - 2z_2),
\end{aligned} \tag{29}$$

where (x_1, y_1, z_1) and (x_3, y_3, z_3) are the signals of the two uncoupled Lorenz systems.

Time traces of the passive subsystem for various values of D are shown in Fig. 26. For $D > 0.07$, the passive subsystem passes through coherent phases much like those of the full LFPU lattice. This confirms that the back-reaction of the coherent subsystem on its neighbours is not important to the creation of these phases.

However, for larger values of D, the coherent phases become longer, and for $D \approx 0.1$, the passive subsystem becomes completely locked into this phase for the length of the computation. This is unlike the LFPU lattice and indicates that the back-reaction is ultimately

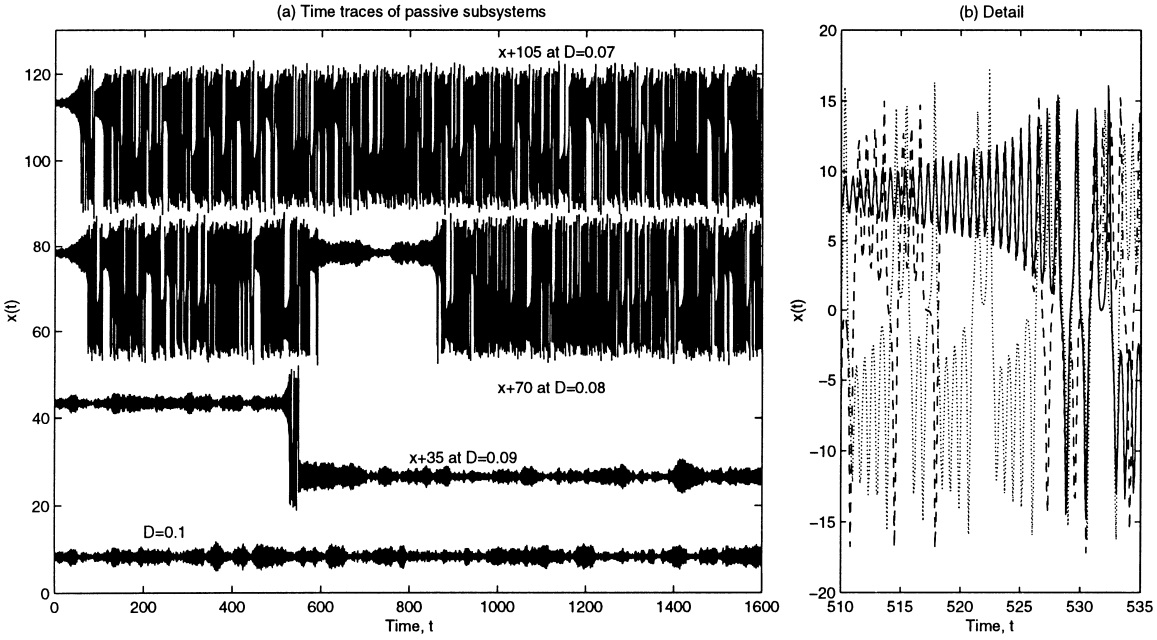

Fig. 26. Time traces of $x_2(t)$ for a passive subsystem driven by two uncoupled Lorenz systems for four different values of D (the curves are diplaced for the purpose of presentation). The sudden switch from the neighbourhood of x_p to that of $-x_p$ for $D = 0.09$ is shown in more detail in panel (b).

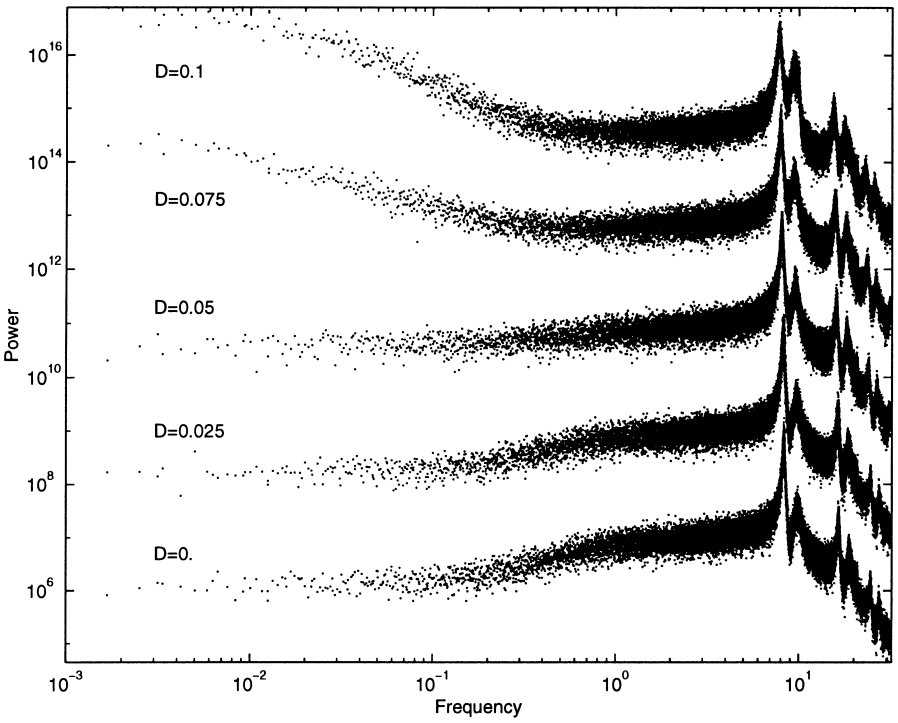

Fig. 27. Lattice-averaged power spectra of z_n for $N = 10$ at $D = 0, 0.025, 0.05, 0.075$ and 0.10. Spectra are plotted against frequency. The spectra are displaced for purposes of presentation.

at least partly responsible for the termination of the coherent phase. There is also some evidence that these events are terminated when one of the driving subsystems spends a prolonged period circulating around one of the butterfly wings (see the detail in panel (b) of Fig. 26).

7.2. Some measures of incoherence

We next compute some more quantitative measures of lattice incoherence. More specifically, we compute power spectra, Lyapunov exponents and the Kaplan–Yorke dimension (e.g. [52]). These measures confirm that the lattices for $D < D_{\rm eg}$ or $D < D_{\rm og}$ are comprised of chaotic, weakly coupled elements.

We display lattice-averaged power spectra for $N = 10$ and five values of D in Fig. 27. For $D = 0$, this amounts to averaging 10 realizations of the Lorenz model. We display the spectra of the z_n-coordinates which show peaks at small period (less than unity) corresponding to the characteristic circulation time around the butterfly wings and its harmonics.

The spectra are all similar at small period (high frequency), reflecting how the shorter timescale variability of the lattice is approximately described by a weakly perturbed Lorenz system. At longer period, there is a significant increase in power as we raise D. This corresponds to the onset of the coherent phases, as shown in Fig. 25. The transition between spectra that are dominated by the Lorenz-like, small-period peak and the spectra that are reddened by the coherent phases takes place between $D = 0.05$ and $D = 0.075$ in line with our previous arguments. In biological contexts, much emphasis is placed on the observation of red spectra in the time series of real populations; this has in the past been explained in terms of enviromental fluctuations of the parameters of a chaotic system [53]. Here we see that spatial coupling of chaotic elements can also redden a spectrum that is otherwise dominated by a short-period peak (see also [54]).

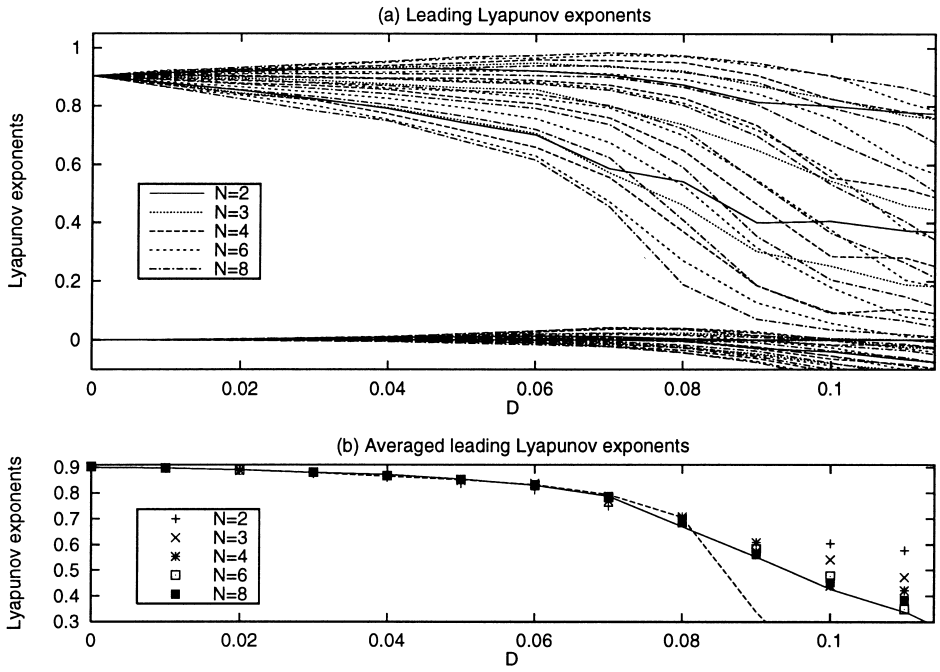

Fig. 28. Leading Lyapunov exponents for $N = 2$, 3, 4, 6 and 8. In panel (b) we display the average of the N leading exponents. This average is roughly independent of N and coincides approximately with the leading Lyapunov exponent of a single subsystem driven passively by two Lorenz systems (dashed line), and of a subsystem on the $N = 8$ lattice, computed assuming the nearest neighbours to provide a fixed driving signal (solid line).

The leading Lyapunov exponents of lattices with $N = 2$, 3, 4, 6 and 8 are shown in Fig. 28. At $D = 0$, we have N uncoupled Lorenz systems and so there are N positive exponents with $\lambda \approx 0.9$, and N exponents that are identically zero (corresponding to time translation symmetry). For finite coupling strengths, only one of this second set of exponents remains zero, since in the coupled system there is only a single trajectory; the remaining exponents become finite. Interestingly, several become positive indicating that there are more positive Lyapunov exponents for the coupled lattice. Thus, based on this discriminant alone, the coupled lattice would appear to be more chaotic than the uncoupled system. More refined measures (as we show below), however, do not share this property.

A second interesting feature of the Lyapunov exponents is that the average of the N leading exponents is approximately independent of N (see Fig. 28b). We attribute this behaviour to the fact that the subsystems are weakly coupled and that they evolve relatively independently. As a result, each is approximately characterized by a single Lyapunov exponent that is a function only of coupling strength. In fact, this "average" exponent approximately corresponds to the leading Lyapunov exponent of the passive subsystem considered above, and to the leading exponent of a subsystem on the $N = 8$ lattice assuming that the coupling to the nearest neighbours is a fixed driving signal (see Fig. 28).

A more quantitative measure of the independence of the lattice size is given by the Kaplan–Yorke dimension. As shown in Fig. 29, when we scale this dimension by the lattice size, it is almost independent of N. We also verified this approximate scaling with lattice size by computing correlation dimensions. In other words, each subsystem must be characterized by a certain dimension; as we add more subsystems to the lattice, we simply add correspondingly more dimensions. The characteristic Kaplan–Yorke dimension of a subsystem is apparently little different to that of the

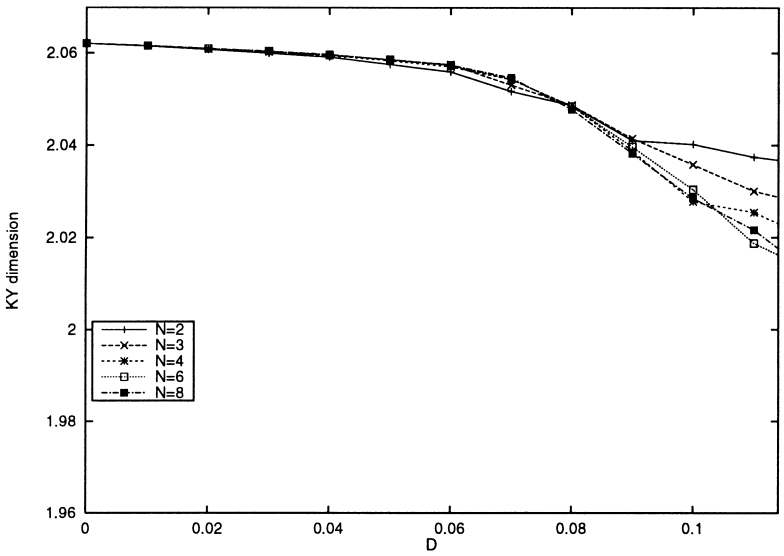

Fig. 29. Scaled Kaplan–Yorke dimension for $N = 2$, 3, 4, 6 and 8. The dimension is scaled by N in order to collapse the data almost to a common curve.

Lorenz system (the vertical scale in Fig. 29 is relatively small). The main reason for this property is that the Lyapunov exponents that are not displayed in Fig. 28 are substantially larger in magnitude and negative. Thus the Kaplan–Yorke dimension basically counts only the number of relatively small Lyapunov exponents; that is, the number of weakly unstable or stable directions on the attractor (which is $2N$). The scaled correlation dimension showed a little more variation with D, but it also is less accurately determined.

The scaling of the characteristic properties with the number of subsystems is indicative that the weakly coupled lattice is an example of an "extensive" system [55].

7.3. Pinning lattice sites; the coherent horizon

The measures computed above confirm that the lattice as a whole is effectively incoherent for small D. Nevertheless, a subsystem influences the surrounding elements; this is the origin of the coherent blocks that are evident in Figs. 22 and 23. A natural question that this observation raises is, how far along the lattice can subsystems affect one another? This distance is a "dynamical horizon" beyond which the lattice elements cannot "know" about one another, and must exist if the lattice dynamics is independent of the lattice size N. A natural way to characterize the dynamical horizon is therefore in terms of cross correlations. We consider that statistical measure in Section 7.4. First, however, we describe computations that highlight this special distance.

To bring out the dynamical horizon, we evolve a lattice, and then abruptly "pin" one of the subsystems at the point $(-x_p, -y_p, z_p)$ corresponding to the coherent phase. This pinning creates a signal that propagates into the lattice, affecting principally the neighbouring sites. An example is shown in Fig. 30. The limited extent of the signal reflects the horizon.

For the particular coupling strength used in this computation, neighbouring subsystems synchronize to the pinned system, and the next nearest neighbours become entrained nearby. The remainder of the lattice, however, evolves much as before. Consequently, the pinning nucleates a "crystal" of coherent subsystems in the lattice much like the briefly coherent synchronized blocks that appear on the free lattice. Evidently, if a subsystem falls into the coherent phase, it exerts a stabilizing mean effect on its neighbours, germinating the synchronized crystal or block. Because the crystal

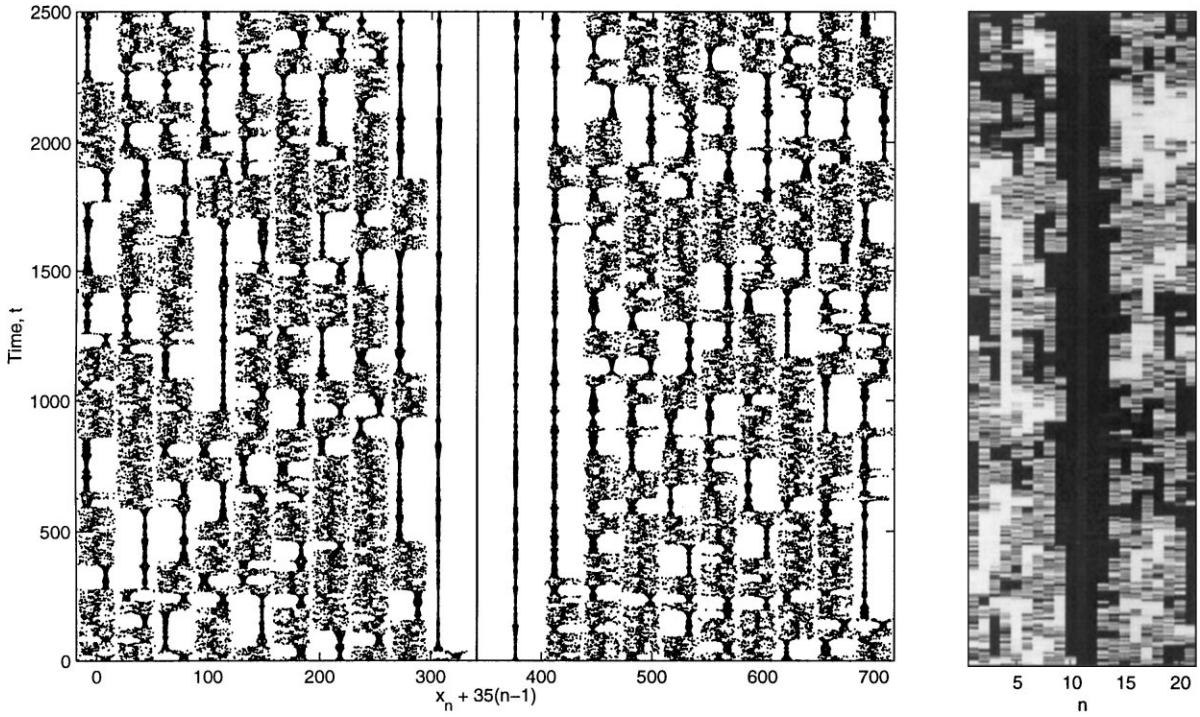

Fig. 30. A lattice of size $N = 21$ with the pinned system $n = 11$ at $D = 0.1$. The first picture shows the time series of x_n; the second displays the running average (of length 5) of x_n, with shading corresponding to level as in Fig. 23.

of coherence has a finite size, we may define a dynamical horizon in terms of the "range of influence" of the pinned subsystem. We measure this range in terms of the mean value of x_n. For the free lattice, this mean value, $\langle x_n \rangle$, vanishes (by symmetry). But $\langle x_n \rangle = -x_p$ for the pinned system, and the mean value of the neighbours is depressed by the synchronizing effect of the coupling. We show $\langle x_n \rangle$ against n and D for a lattice with $N = 21$ in Fig. 31.

For small coupling strengths, the pinning has little effect on the other lattice sites and the mean values remain close to zero. For larger D, the mean values of the surrounding lattice sites become negative. Once $\langle x_n \rangle < 2.55$, we define the site to be in the range of influence of the pinned site. This leads to the picture shown in Fig. 31b. The threshold value is arbitrary, and was chosen primarily to lie above any fluctations in the average in the "uninfluenced" parts of the lattice. These fluctations are rather large in a finite-length computation because of the presence of the coherent phases; for longer runs the fluctuations are smaller, and in principle, we could define a wider horizon. We return to this point in Section 7.4.

The central feature of the pinning computation is that it describes how a subsystem that is forced to remain coherent affects the rest of the lattice. Thus, what we identify as the range of influence is essentially that for a coherent phase. In other words, the results shown in Fig. 31 reflect a "coherent horizon". This horizon is likely to be farther than the true dynamical horizon because the coherent subsystem affects its neighbours through the mean value of all of x_n, y_n and z_n. But for an incoherent system, the average value of x_n and y_n is zero, and so the long-time effect is much reduced.

7.4. Cross correlations; incoherent horizons

A more quantitative measure of the degree to which the subsystems influence one another comes from the

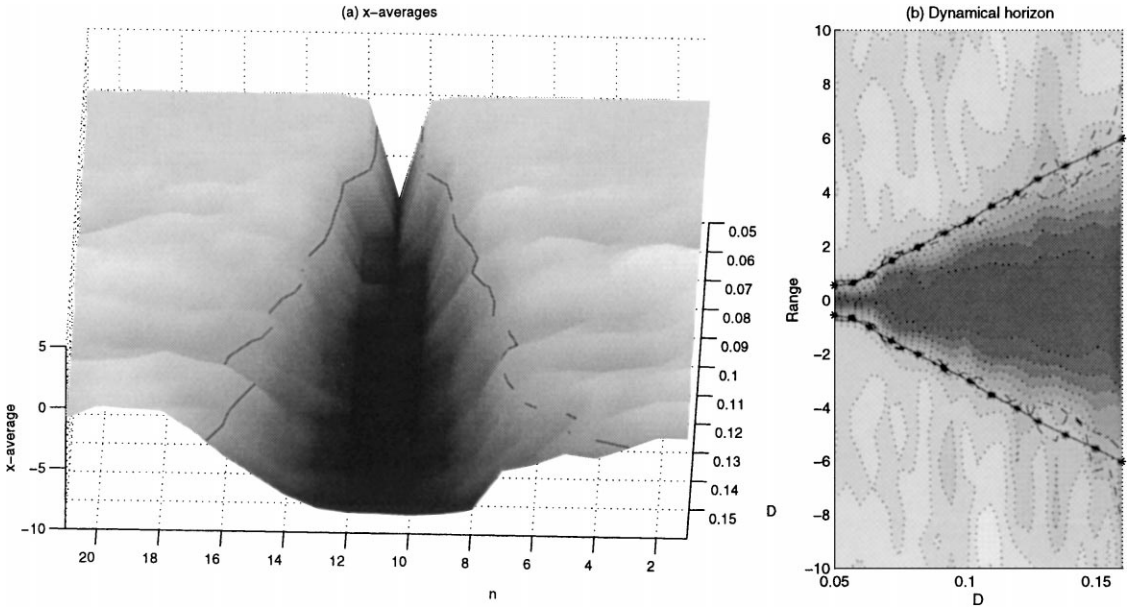

Fig. 31. (a) Average values of x_n for a lattice with a pinned $n = 11$ site over computational runs of length 2×10^4. Values of D between 0.05 and 0.11 in steps of 0.005 are displayed. The lines show the level $\langle x_n \rangle = -2.55$. In (b), the averages are shown as shaded contours on the (D, n) planes. The dashed contours show the level $\langle x_n \rangle = -2.55$, and the dash-dotted contours show the same, but reflected about the $n = 11$ lattice site. The solid line and stars display our estimate of the dynamical horizon based on these pairs of contour lines.

cross correlation:

$$C_{i,j} = \frac{\langle x_i x_j \rangle}{\sqrt{\langle x_i^2 \rangle \langle x_j^2 \rangle}}, \tag{30}$$

where the angled brackets indicate the temporal average. (Practically we replace the denominator by $\langle x_i^2 \rangle$ since the lattice sites have identical mean values.) For uncorrelated subsystems, $C_{i,j} = 0$, and $C_{i,i} = 1$.

We show the cross correlation as a function of distance between two sites on the lattice (that is, $C_{n,n+m}$ against m, averaged over n) in Fig. 32. The correlation between two subsystems falls off quickly with their separation along the lattice, and the correlation is rapidly lost in the sea of error introduced by the finite-length computation. Unsurprisingly, lattices with smaller coupling show less correlation.

What is perhaps more surprising is that the trend of the correlation is well approximated by $C_{n,n+m} \approx C^m_{n,n+1}$. That is, the correlation roughly follows a simple power law. This kind of behaviour can be rationalized if we interpret the interaction in a more probabilistic fashion. That is, if we interpret the correlation $C_{n,n+1}$ as the probability that a site is affected by the nearest neighbour. Then a natural estimate of the probability that the nearest neighbour affects our lattice point is $C^2_{n,n+1}$, and so forth.

This observation, however, obscures the meaning of the dynamical horizon: there is no cut-off in the correlation at finite distance along the lattice for an error-free computation with infinite length. Indeed, according to Takens' theorem [56], one should be able to reconstruct the attractor given access to an arbitrarily long time series.[3] However, physical time series have finite length, and this is reflected in precision in phase space: due to close returns, the longer the computation is, the smaller the phase-space scales that are

[3] There is no pressing reason why the coordinate of a weakly coupled subsystem is not generic; the information about the rest of the lattice is simply contained in small amplitude fluctuations and the lattice dimension is very large.

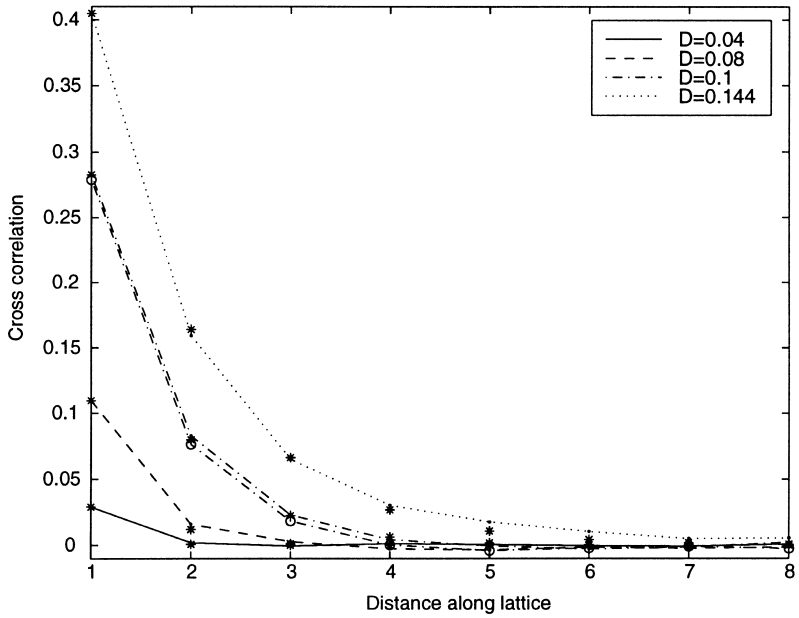

Fig. 32. Cross correlations, $C_{n,n+m}$, plotted against distance along the lattice, m, and averaged over n. This figure displays results for a lattice of size $N = 50$, but the correlations are essentially the same for smaller lattices, as illustrated by the result for $N = 20$ and $D = 0.1$ which is also included (shown by the dash-dotted lines and circles). The stars show $C^m_{n,n+1}$; that is, the nearest neighbour correlation raised to the power m.

explored by the system. Thus, there is always some small-scale cut-off in phase space because of the finite length of the computation. Practically, this sort of limitation is the origin of the horizon, and there is no conflict with the embedding theorem. In other words, the dynamical horizon is a function of the duration of the computation.

With this image in mind, we define the horizon in terms of the length of the computation. We measure the "precision" by evolving two independent (uncorrelated) lattices and computing $C_{n,n+m}$ with $x_n(t)$ and $x_{n+m}(t)$ taken from the different lattices, and then averaging over as many values of n and m as were used in the computation of Fig. 32. This provides a mean correlation, $\bar{c}(T)$, and variance, $\bar{v}(T)$, that are functions of the length of the computation, T. Both tend to zero as $T \to \infty$. From the mean and variance we construct an estimate of the precision, $\varsigma(T) = \bar{c}(T) + 3\bar{v}(T)$ (giving a 95% level of confidence).

Then, in order to observe the correlation at a distance m along the lattice, the actual correlation must exceed the precision, and so

$$C_{n,n+m} \approx C^m_{n,n+1} > \varsigma(T)$$
$$\text{or} \quad m < m_c(T) = \frac{\log \varsigma(T)}{\log C_{n,n+1}}. \tag{31}$$

We illustrate this criterion in Fig. 33.

From the figure we read off the horizon for various values of T. For example, with $T = 2 \times 10^4$ we find a horizon of $m = 3$ for $D = 0.1$. The horizons evident from Fig. 33 approximately coincide with our cruder estimates in Fig. 31.

An alternative definition of cross correlation to (30) is provided by using the z_n coordinates rather than x_n:

$$\tilde{C}_{i,j} = \frac{\langle (z_i - \bar{z})(z_j - \bar{z}) \rangle}{\langle (z_i - \bar{z})^2 \rangle}, \tag{32}$$

where $\bar{z}$ is the average value of z_n. We mention this alternative estimate of the correlation because it shows an interesting difference with that defined by (30). More specifically, the alternative definition predicts much smaller correlations for larger values of D (by

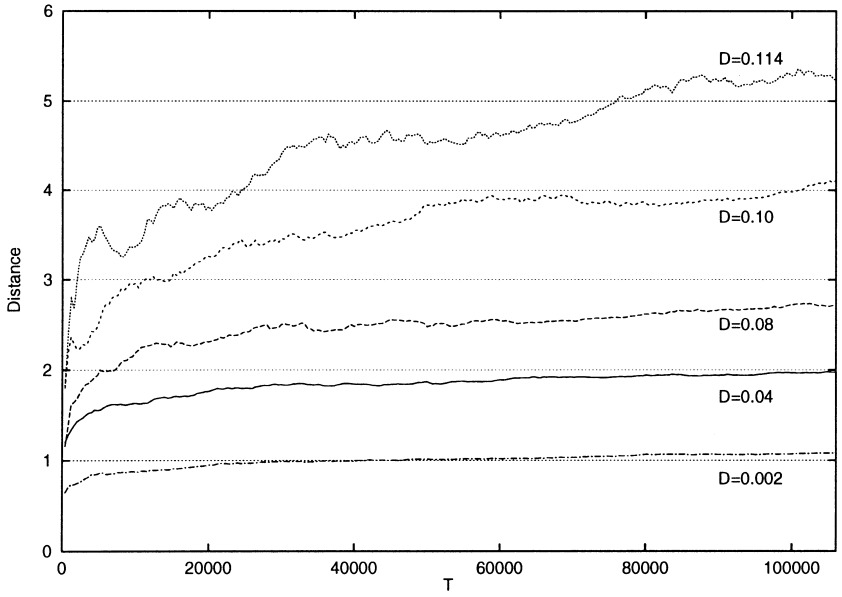

Fig. 33. Dynamical horizon estimates. Displayed is the distance, $m_c(T)$, defined in (31) against T, the length of the computational run, for $D = 2 \times 10^{-3}$, 0.04, 0.08, 0.1 and 0.114. Distances below these curves are within the dynamical horizon.

a factor of about 3 at $D = 0.1$); for smaller coupling strength, the two definitions predict comparable correlations.

The reason behind the difference lies in the fact that the alternative definition is based on the variation of z_n about its mean value. But that mean value lies near z_p, the value of z_n characterizing the coherent phases. Thus, when a system falls into a coherent phase, its contribution to the cross correlation in (32) is anomalously small compared to how it contributes to (30). But it is these phases that are most effective in the lattice interactions because of their large (running) mean values, and so they can provide significant contributions to the correlation. In other words, the alternative definition is biased against the coherent phases, and this reduces the observed correlations. Moreover, because the phases are predominant only at larger coupling strengths, when D is small the differences between (30) and (32) should be less pronounced, as is observed.

In other words, the results derived from using (32) lie closer to the values expected if we removed the coherent phases. Thus, we measure something closer to an "incoherent horizon". Similar arguments to those used to construct Fig. 33 then lead to estimates of the horizon that are never further than the neighbouring lattice site.

8. Discussion

The LFPU experiment is very different from the Fermi–Pasta–Ulam experiment from which we coined the name. This is perhaps not so surprising in view of the fundamental differences in the dynamics of the uncoupled elements. An essential difference between the two is that the Fermi–Pasta–Ulam chain is a conservative system, whereas the LFPU lattice is very dissipative. All in all, rather than coherent, travelling excitations, the LFPU system shows a variety of low-dimensional dynamics including synchronized chaos, spatially structured, steady equilibria, and time-dependent states with time-averaged spatial structure. In addition, when coupling is weak, the lattice shows high-dimensional incoherence.

By way of a summary, we now return to Fig. 5, which encapsulates many of our results. This regime diagram provides a concise summary of the parameter regimes in which we encounter various types

of dynamical behaviour. First, the results of the initial-value problems give some idea regarding what attractors might result from initial states of low amplitude. Due to the presence of the many multiple equilibria, however, the picture portrayed by these results is very incomplete. To gain a more complete image, we turn to the curves also drawn in Fig. 5.

The line $D = D_S(N)$ gives the lower limit of synchronization: below this line, synchronized states are unstable (this boundary may not be very distinct [22]). Stable steady equilibria may be found over the ranges $D_{eg} < D < D_0(N)$ or $D_{og} < D < D_0(N)$, depending on whether the number of lattice sites is even or odd. The fact that the lower limits of stable equilibria in Fig. 5 for even and odd lattices (D_{eg} and D_{og}) are so different suggests that lattices with even N are quantitively different to those with odd N. This suggestion is probably misleading for two reasons. First, although the steady states and their stability are different for even and odd N, the time-dependent lattice dynamics is not obviously so: over the range $D_{eg} < D < D_{og}$, provided the system does not converge to one of these equilibria, the lattice dynamics appears to be similar for even and odd N. Second, from a physical perspective it is often more relevant to consider lattices with a fixed spatial size but varying degree of discretization. Such lattices are obtained from our system (1)–(3) by rescaling the discrete variable by N. Then, the diffusivity becomes $\tilde{D} = D/N^2$, and so the points of stability, D_{eg} and D_{og}, scale as N^{-2}. Hence, these rescaled diffusivities decrease with N, and so the suggestion of a fundamental difference is, in this sense, misleading.

The extent of time-dependent attractors is substantially more difficult to estimate, since it is probably given by the saddle-node bifurcation with the largest coupling strength. Very roughly we estimate the upper limit by $D = D_H(N)$, the location of the Hopf bifurcation that destabilizes the A_1 branch of steady equilibrium solutions. For larger N, this is the first Hopf bifurcation to occur and so generates the first unstable oscillatory branch. That branch is probably the one that turns around at the largest coupling strength. Thus stable time-dependent states may well begin to exist at values of D just above this curve.

The other noteworthy boundary in Fig. 5 is $D = D_t$, the line along which the pseudo-translation eigenvalue of the symmetrical equilibria exceeds 10^{-3}, signifying the emergence of the effects of discreteness. At first it appears peculiar that the threshold is independent of N and that we cannot refine the lattice to better achieve a continuum. But, again, this is because our system size is not fixed as we vary N: discreteness becomes important when $\tilde{D} < D_t/N^2$, for systems of fixed size. Thus adding elements makes the lattice more like a continuum, as expected.

This concludes our study of the LFPU experiment. So far, our study has been rather abstract, and we have avoided any proper discussion of real issues. We close in this vein and mention only some potential applications of our results.

8.1. Discreteness

One motivation we cited in Section 1 was to climate dynamics. But one of the aspects of this application is not to the climate problem directly, but to the sophisticated numerical schemes that are used for simulations: GCMs. One of the main features of these codes is that they attempt to incorporate many of the physical ingredients to the climate problem in all three of its dimensions. One consequence of this massive input to the problem is that the codes cannot be particularly well resolved. Instead, they may be based on a relatively coarse computational grid. As such, effects of discreteness may enter the problem (e.g. [57]).

For our LFPU lattice there are some notable effects of discreteness. One of the most obvious is the presence of the "grid mode", the steady equilibrium solutions that remains stable at the smallest coupling strengths. This mode is different in even and odd lattices, leading to some peculiar differences between the two (but see the remarks above).

But perhaps a more important effect of discreteness is the way it allows weakly coupled lattices to become incoherent. For the relatively small lattices we consider, only low dimensional temporal dynamics is observed at the coupling strengths where the lattice is not very discrete. High dimensional, temporal chaos only appears for weak coupling. This warns us that

the phenomenon that one might be tempted to identify as "turbulence" is really a property of the discrete lattice and not of the related continuum system. Likewise, full synchronization is always unstable in sufficiently large continuous systems, but it is one of the key features of the discrete LFPU chain at large coupling strength.

Another remark that one might make in this regard is that when we are in the incoherent regime, the system is independent of the lattice size, N. This is precisely the feature that is desired of numerical schemes for PDEs. However, the desired property does not arise because we solve the continuum properly, but, in fact, reflects a fundamentally different aspect of the numerical problem.

A related issue arises in theories of friction and stick-slip phenomena, and in earthquake models. In these models, it appears that much of the complicated dynamics arises purely as a result of effects of discreteness [10,58]. But whether this implies that there is a serious physical flaw in the models is not so clear, because one might argue that microscopic heterogeneity is important in introducing effects like discreteness.

8.2. Issues of predictability

Perhaps the most relevant application of the LFPU dynamics is to the issue of reconstruction and predictability in very complicated physical systems (such as the climate). The computations described in Section 7 all point to the fact that in the weakly coupled limit, the interaction between the LFPU subsystems is close-range; that is, beyond a dynamical horizon that depends on the computation time, the subsystems have no knowledge of one another and the dynamics is independent of the lattice size. This feature has disturbing implications regarding the predictability of the lattice: given information about only a single element, it would not seem possible to predict the dynamics of the entire LFPU system unless one had an arbitrarily long, error-free time series. This barrier to predictability was previously described by Lorenz [5] in the context of a simple climate model, and expanded upon further by von Hardenberg and Provenzale [8].

We have explored the issue somewhat further using the LFPU lattice. More specifically, we have taken time series from the subsystems and then treated it as experimental or observational data. From this data, we used standard techniques to reconstruct the correlation dimension of the system. Since we know what the real phase space of the system is and can determine the correlation dimension directly, the time series provided synthetic data to test the reconstruction. The signal from a single subsystem (such as the time series of $z_n(t)$ for a particular n) produced a correlation dimension as a function of embedding dimension that appeared to saturate at a certain, low value. However, a careful inspection indicated that it also continued to increase, albeit much more slowly, in larger embedding spaces. In other words, the signal looked as though it might converge at a misleadingly small estimate of the dimension, but really did not converge. The computation therefore mirrored the results of Lorenz and von Hardenberg and Provenzale.

A time series constructed from many of the subsystems (such as $\sum_n z_n(t)$), however, fared better; it simply failed to converge. In other words, whilst this test did not give an incorrect positive result, it facilitated no conclusion at all. The reason behind this failure is essentially that in order to determine the dimension of a system as large as one of our weakly coupled, LFPU lattices, we need a ridiculously long time series; a time series that is of an impractically long length. Hence methods that attempt to reconstruct the phase space and then estimate statistical measures such as dimension are simply not useful in this context. Based on results such as these, we see no reason to believe in any of the predictions of low-dimensional attractors in extensive natural systems, but this remark has been made before.

An alternative approach to predictability is not to try to reconstruct the whole system, but to assess how the growth of an error in one of the subsystems becomes spread across the lattice. That is, if we suddenly disturb one of the subsystems, when is the disturbance recorded at another lattice site (if at all). Clearly this has some relation to the concept of the dynamical horizon that we have discussed above, but it also bears on questions of an initial-value flavour. This calcula-

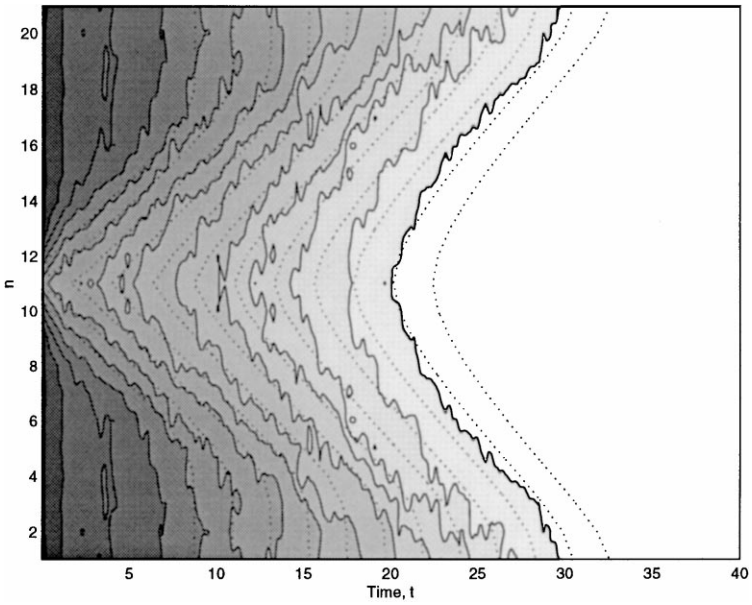

Fig. 34. The propagation of an error between two lattices that are initially identical but for a difference in the value of x_{11} of 10^{-8}. The lattice size is $N = 21$ and $D = 0.05$. Shown is a contour plot of the error, $[(x_n - x'_n)^2 + (y_n - y'_n)^2 + (z_n - z'_n)^2]^{1/2}$, averaged over 63 different realizations of the computations, and also on exploiting the symmetry, $n \to 11 - n$. The dotted lines show contours of the solution to Eq. (33).

tion enables us to estimate, for example, how our lack of knowledge of the behaviour of some elements ultimately limits our ability to forecast the future of the system (see also [7]).

To compute this propagation of error we take two identical, evolved lattices, then suddenly introduce a perturbation into the x_n coordinate of one of the subsystems of one lattice. This difference precipitates a divergence in the subsequent evolution of the two lattices, and we measure the differences, or error, in each of the subsystems. The result of such a computation is shown in Fig. 34.

For this computation, we introduce an error in the eleventh subsystem of a lattice with $N = 21$. Due to different round-off errors in all the subsystems of the two lattices, we also immediately introduce a global error of order 10^{-14}, dictated by the finite precision of the computation. Both the local error at $n = 11$ and the global error subsequently grow due to the hallmark of chaos: exponential separation of neighbouring trajectories. Because the initial local error is so much larger and since the lattice has finite size, the global error is eventually swamped by that propagating from the distinguished lattice site. This leads to the characteristic "V-shape" in Fig. 34. Also, ultimately, the error in phase space is limited by the size of the attractor, and we reach a finite maximal error.

The propagation and growth of the error is well approximated by the solution to the linear system (see Fig. 34)

$$\frac{\mathrm{d}x_n}{\mathrm{d}t} = D(x_{n+1} + x_{n-1} - 2x_n) + \lambda x_n \tag{33}$$

with the initial condition

$$x_n(t = 0) = 10^{-12} + 10^{-8}\delta_{n,11}, \tag{34}$$

where λ is a linear growth rate. Practically, we use $\lambda = 1.05$, which is close to the maximum Lyapunov exponent of this particular lattice. In other words, the error propagation can be approximately described by the overall growth due to chaotic separation, as measured by λ, and the discrete diffusion across the lattice.

The continuum limit of Eq. (33) has a similarity solution of the form

$$x(n,t) = \frac{A}{\sqrt{t}}\exp\left[\lambda t - \frac{1}{4Dt}(n-11)^2\right] \tag{35}$$

in the instance that the initial error is purely local. If we ignore the more slowly varying, time-dependent factor outside the exponential, then we observe that a characteristic speed of propagation for the error is given by $2\sqrt{\lambda D}$. This speed reproduces the linear portions of the curves in Fig. 34.

8.3. Extensions

Some extensions of the present work include generalizing the LFPU lattice so that the subsystems are no longer identical, introducing the effects of deterministic parameter fluctuations or noise, and changing the form of the coupling.

To address the first issue we conducted a cursory study like the preliminary initial-value computations reported in Section 3. To generate inhomogeneous lattices we introduced the parameter variation, $r_n = 28 + \epsilon_n$, where ϵ_n was randomly chosen between $[-1, 1]$. For $N = 20$, the results were not qualitatively different for $D < D_S$: equilibrium states, their radiative instabilities and incoherent lattices all appeared at roughly the same coupling strengths. This observation is not especially surprising in view of the fact that the qualitative properties of the equilibria and the weakly coupled subsystems do not hinge on the subsystems being identical.

What does change, however, is the behaviour for coupling strengths at which the homogeneous lattice synchronizes. When $\epsilon_n \neq 0$, there is no longer an invariant, synchronization manifold, and the lattice cannot converge to global synchrony. Instead, in the initial-value computations, the system tends to a state that is almost synchronous in the sense that each individual orbit is similar, but there are O(1) differences in the coordinates, (x_n, y_n, z_n) (see Fig. 35). This state is similar to the phase-synchronized Rossler systems considered by Osipov et al. [21]. However, the state does not appear to persist indefinitely. Occasional desynchronizing events drive the system away from this state (as in the event near $t = 10.5$ in Fig. 35b; the events are evidently associated with close passage by the origin). The result of this desynchronization is that the system is eventually captured by a steady equilibrium, provided one is stable. If $D > D_0$, on the other hand, the system recovers some degree of synchrony after a brief burst of disorder.

This dynamics is especially sensitive to slight difference in the initial-value computations. In fact, it is not clear whether slight errors play a dominant role in determining the ultimate fate of the system. This type of behaviour is known in lower dimensional systems, and is associated with the complicated geometry of the phase space in the vicinity of where the synchronization manifold once was [59,60]. The main feature of the dynamics elucidated in those studies is that arbitrarily small differences in the subsystems can produce sporadic desynchronizations, and arbitrarily small differences in initial conditions can change the state to which the system ultimately converges (there are "riddled" basins of attraction). We conjecture that these features are also common to the inhomogeneous LFPU lattice.

For related reasons, it is likely that adding deterministic parameter fluctuations or noise to homogeneous lattices has a similar effect on the synchronized state. The steady states are also subject to perturbation in this instance, but provided the disturbances are small, there is no pressing reason to suppose that the states are completely destroyed. Rather, the lattice may simply fluctuate near the unperturbed equilibria. These kinds of perturbations may model additional internal degrees of freedom. Once the lattice is incoherent, it is plausible that the additional degrees of freedom affect the mean properties of each subsystem, but not the fact that the system as a whole is incoherent.

We have not undertaken any studies that attempt to address the question of how changing the coupling modifies the lattice dynamics, chiefly for fear of opening Pandora's Box. However, we may still ask the question of what features of the lattice dynamics might change in such a modification to the LFPU system. For example, synchronized states can become susceptible to different types of instability [20]. Notably, it is no longer true that the systems must always synchro-

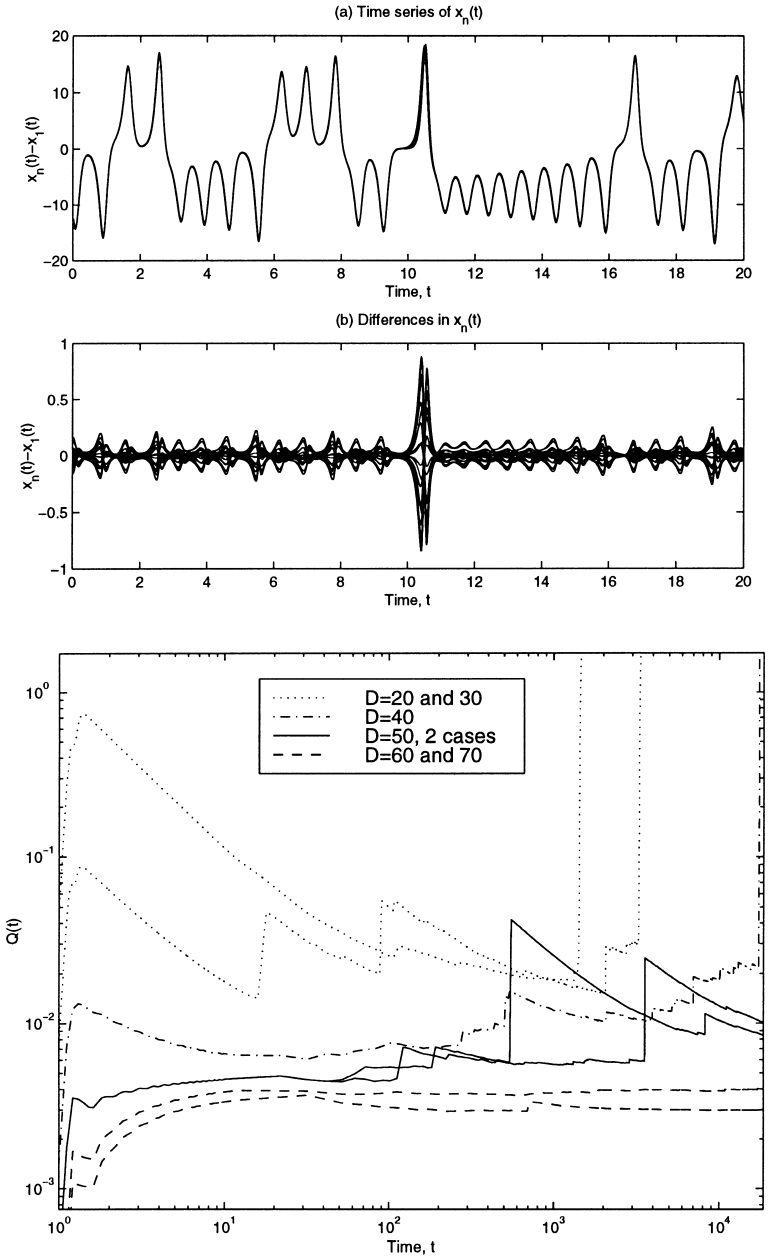

Fig. 35. Pseudo-synchronization in a nonidentical lattice. Panels (a) and (b) show time series of $x_n(t)$ and $x_n(t)-x_1(t)$ for $N = 20$ and $D = 15$ and every n. In panel (c) we display evolution over longer timescales. Shown is the quantity $Q(t) = t^{-1}(N-1)^{-1}\int_0^t \sum_{n=2}^{N}[x_n(s)-x_1(s)]^2\,\mathrm{d}s$. This integral mean-square difference does not converge to zero. For $D = 20$, 30 and 40, the system ultimately diverges from a phase-synchronized state to a steady equilibrium.

nize at sufficiently large D. The steady equilibria may also no longer exist; such states are not observed in the coupled Rossler systems in [19,21]. However, the incoherent limit is not likely to be very different (we have verified that the behaviour of passive subsystems is relatively insensitive to the precise form of the coupling). Thus, only weakly coupled incoherence may survive a change in the form of the coupling.

Acknowledgements

NJB thanks Charles Tresser and Chai-Wah Wu for discussions in the early stages of this work, and the Nuffield Foundation for an equipment grant. We thank the ISI Foundation (Torino) for hospitality during part of this work.

References

[1] E. Fermi, J.R. Pasta, S. Ulam, Studies of nonlinear problems, Los Alamos Report LA-1940, 1955.
[2] N.J. Zabusky, M.D. Kruskal, Interaction of solitons in a collisionless plasma and the recurrence of initial states, Phys. Rev. Lett. 15 (1965) 240.
[3] E.N. Lorenz, Deterministic nonperiodic flow, J. Atmos. Sci. 20 (1963) 130.
[4] E.A. Spiegel, in: W. Malkus, F.J. Mellor (Eds.), Geophysical Fluid Dynamics, vol. WHOI-81-102, Woods Hole Oceanographic Institution, 1981, pp. 1–77.
[5] E.N. Lorenz, Dimension of weather and climate attractors, Nature 353 (1991) 241.
[6] E.N. Lorenz, in: Proceedings of the Seminar on Predictability, vol. 1, ECMWF, Reading, Berkshire, UK, 1996.
[7] E.N. Lorenz, K.A. Emanuel, Optimal sites for supplementary weather observations: simulation with a small model, J. Amtos. Sci. 55 (1998) 399.
[8] J. von Hardenberg, A. Provenzale, in: G.C. Castagnoli, A. Provenzale (Eds.), Proceedings of the International School of Physics “Enrico Fermi”, vol. 133, IOS Press, Amsterdam, 1997, pp.161–176.
[9] R. Burridge, L. Knopoff, Model and theoretical seismology, Bull. Seismol. Soc. Am. 57 (1967) 341.
[10] J.M. Carlson, J.S. Langer, Mechanical model of an earthquake fault, Phys. Rev. A 40 (1989) 6470.
[11] F. Helot, T. Baumberger, B. Perrin, B. Caroli, C. Caroli, Creep, stick-slip and dry-friction dynamics: experiments and a heuristic model, Phys. Rev. E 49 (1994) 4973.
[12] B.N.J. Persson, Theory of friction: stress domains, relaxation and creep, Phys. Rev. B 51 (1995) 13568.
[13] R.C. Elson, A.I. Selverston, R. Huerta, N.F. Rulkov, M.I. Rabinovich, H.D.I. Abarbanel, Synchronous behaviour of two coupled biological neurons, Phys. Rev. Lett. 81 (1998) 5692.
[14] H. Sompolinksy, D. Golomb, D. Kleinfel, Cooperative dynamics in visual processing, Phys. Rev. A 43 (1991) 6990.
[15] A.T. Winfree, The Geometry of Biological Time, Springer, Berlin, 1980.
[16] Y. Kuramoto, Chemical Oscillations, Waves and Turbulence, Springer, New York, 1984.
[17] A. Turing, Philos. Trans. R. Soc. London B 237 (1952) 37.
[18] L. Brunnet, H. Chaté, P. Manneville, Long-range order with local chaos in lattices of diffusively coupled ODEs, Physica D 78 (1994) 141.
[19] J.F. Heagy, T.L. Carroll, L.M. Pecora, Synchronous chaos in coupled oscillator systems, Phys. Rev. E 50 (1994) 1874.
[20] J.F. Heagy, T.L. Carroll, L.M. Pecora, Short-wavelength bifurcations and size instabilities in coupled oscillator systems, Phys. Rev. Lett. 74 (1995) 4185.
[21] G.V. Osipov, A.S. Pikovsky, M.G. Rosenbaum, J. Kurths, Phase synchronization effects in a lattice of nonidential Rössler oscillators, Phys. Rev. E 55 (1997) 2353.
[22] L.M. Pecora, T.L. Carroll, G.A. Johnson, D.J. Mar, J.F. Heagy, Fundamentals of synchronization in chaotic systems, concepts, and applications, Chaos 7 (1997) 520.
[23] A.S. Pikovsky, M.G. Rosenblum, J. Kurths, Synchronization in a population of globally coupled chaotic oscillators, Europhys. Lett. 34 (1996) 165.
[24] D.H. Zanette, A.S. Mikhailov, Condensation in globally coupled populations of chaotic dynamical systems, Phys. Rev. E 57 (1998) 276.
[25] X.J. Wang, J. Rinzel, Alternating and synchronous rhythms in reciprocally inhibitory model neurons, Neural Comput. 4 (1992) 84.
[26] X.J. Wang, J. Rinzel, Spindle rhythmicity in the reticularis thalami nucleus: synchronization among mutually inhibitory neurons, Neuroscience 53 (1993) 899.
[27] D. Golomb, J. Rinzel, Dynamics of globally coupled inhibitory neurons with heterogeneity, Phys. Rev. E 48 (1993) 4810.
[28] D. Golomb, J. Rinzel, Clustering in globally coupled inhibitory neurons, Physica D 72 (1994) 259.
[29] R. Huerta, M. Bazhenov, M.I. Rabinovich, Clusters of synchronization and bistability in lattices of chaotic neurons, Europhys. Lett. 43 (1998) 719.
[30] K. Kaneko, Clustering, coding, switching, hierarchical ordering, and control in a network of chaotic elements, Physica D 41 (1990) 137.
[31] K. Kaneko, Partition complexity in a network of chaotic elements, J. Phys. A 24 (1991) 2107.
[32] N.J. Balmforth, A. Jacobson, A. Provenzale, Synchronized family dynamics in globally coupled maps, Chaos 9 (1999) 738.
[33] M.G. Rosenblum, A.S. Pikovsky, J. Kurths, Phase synchronization of chaotic oscillators, Phys. Rev. Lett. 76 (1996) 1804.
[34] Y.-H. Qian, D.-H. Feng, Diffusive Lorenz dynamics: coherent structures and spatio-temporal chaos, Preprint, 1998.
[35] P. Coullet, C. Tresser, C.-W. Wu, The diffusive Lorenz equations, Preprint, 1998.
[36] P. Ashwin, J. Buescu, I. Stewart, From attractor to chaotic saddle: a tale of transverse stability, Nonlinearity 9 (1994) 703.
[37] H. Fujisaka, T. Yamada, Stability theory of synchronized motion in coupled-oscillator systems, Prog. Theoret. Phys. 69 (1983) 32.
[38] V.S. Afraimovich, W.-W. Lin, Synchronization in lattices of coupled oscillators with Neumann/periodic boundary conditions, Dyn. Stability Syst. 13 (1998) 237.
[39] M. Peyrard, M.D. Kruskal, Kink dynamics in the highly discrete sine-Gordon system, Physica D 14 (1984) 88.
[40] L.P. Shil’nikov, A case of the existence of a denumerable set of periodic motions, Sov. Math. Dokl. 6 (1965) 163.
[41] N.J. Balmforth, Solitary waves and homoclinic orbits, Ann. Rev. Fluid Mech. 27 (1993) 335.

[42] A.R. Champneys, Homoclinic orbits in reversible systems and their applications in mechanics, fluids and optics, Physica D 112 (1998) 158.
[43] C. Elphick, G.R. Ierley, O. Regev, E.A. Spiegel, Interacting localized structures with Galilean invariance, Phys. Rev. A 44 (1991) 1110.
[44] N.J. Balmforth, G.R. Ierley, R. Worthing, Pulse dynamics in an unstable medium, SIAM J. Appl. Math. 57 (1997) 205.
[45] R.L. Devaney, Reversible diffeomorphisms and flows, Trans. Am. Math. Soc. 218 (1976) 89.
[46] A.R. Champneys, J.F. Toland, Bifurcation of a plethora of multi-modal homoclinic orbits for autonomous Hamiltonian systems, Nonlinearity 6 (1993) 655.
[47] J. Härterich, Cascades of reversible homoclinic orbits to a saddle-focus equilibrium, Physica D 112 (1998) 187.
[48] K. Weisenfeld, P. Hadley, Attractor crowding in oscillator arrays, Phys. Rev. Lett. 62 (1989) 1335.
[49] D. Golomb, D. Hansel, B. Shraiman, H. Sompolinsky, Clustering in globally coupled phase oscillators, Phys. Rev. A 45 (1992) 3516.
[50] N.J. Balmforth, E.A. Spiegel, C. Tresser, Checkerboard maps, Chaos 5 (1995) 216.
[51] N. Platt, E.A. Spiegel, C. Tresser, On–off intermittency: a mechanism for bursting, Phys. Rev. Lett. 70 (1993) 279.
[52] H. Kantz, T. Shreiber, Nonlinear Time Series Analysis, Cambridge University Press, Cambridge, 1997.
[53] N.J. Balmforth, A. Provenzale, E.A. Spiegel, M. Martens, C. Tresser, C.-W. Wu, Red spectra from white and blue noise, Proc. Roy. Soc. London B 266 (1999) 311.
[54] A. White, M. Begon, R.G. Bowers, Explaining the colour of power spectra in chaotic ecological models, Proc. R. Soc. London B 263 (1996) 1731.
[55] T. Bohr, M.H. Jensen, G. Paladin, A. Vulpiani, Dynamical Systems Approach to Turbulence, Cambridge University Press, Cambridge, 1998.
[56] F. Takens, in: D.A. Rand, L.S. Young (Eds.), Lecture Notes in Mathematics, vol. 898, Springer, New York, 1981, p. 366.
[57] P. Cessi, W.R. Young, Some unexpected consequences of the interaction between convective adjustment and horizontal diffusion, Physica D 98 (1996) 287.
[58] H.J. Xu, L. Knopoff, Periodicity and chaos in a one-dimensional dynamical model of earthquakes, Phys. Rev. E 50 (1994) 3577.
[59] S.C. Venkataramani, B.R. Hunt, E. Ott, D.J. Gauthier, J.C. Bienfang, Transitions to bubbling of chaotic systems, Phys. Rev. Lett. 77 (1996) 5361.
[60] S.C. Venkataramani, B.R. Hunt, E. Ott, Bubbling transition, Phys. Rev. E 54 (1996) 1346.